SESSION II

Application of Synchrotron Radiation Techniques and Complementary Techniques

Chairs: P.G. Allen, J.I. Kim, C. Madic, T. Fanghänel, G.H. Lander, N.M. Edelstein

ACTINIDE SCIENCE WITH SOFT X-RAY SYNCHROTRON RADIATION

David K. Shuh
Actinide Chemistry Group, The Glenn T. Seaborg Center
Lawrence Berkeley National Laboratory (LBNL)
MS 70A-1150, 1 Cyclotron Road, Berkeley, CA 94720, USA

Abstract

Several workshops, some dating back more than fifteen years, recognised both the potential scientific impact and opportunities that would be made available by the capability to investigate actinide materials in the vacuum ultraviolet (VUV)/soft X-ray region of the synchrotron radiation (SR) spectrum. This spectral region revolutionised the approach to surface materials chemistry and physics nearly two decades ago. The actinide science community was unable to capitalise on these SR methodologies for the study of actinide materials until recently because of radiological safety concerns. The Advanced Light Source (ALS) at LBNL is a third-generation light source providing state-of-the-art performance in the VUV/soft X-ray region. Along with corresponding improvements in detector and vacuum technology, the ALS has rendered experiments with small amounts of actinide materials possible. In particular, it has been the emergence and development of microspectroscopic techniques that have enabled investigations of actinide materials at the ALS.

The primary methods for the experimental investigation of actinide materials in the VUV/soft X-ray region are the complementary photoelectron spectroscopies, near-edge X-ray absorption fine structure (NEXAFS) and X-ray emission spectroscopy (XES) techniques. Resonant photo-emission is capable of resolving the 5f electron contributions to actinide bonding and can be used to characterise the electronic structure of actinide materials. This technique is clearly a most important methodology afforded by the tunable SR source. Core level and valence band photoelectron spectroscopies are valuable for the characterisation of the electronic properties of actinide materials, as well as for general analytical purposes. High-resolution core-level photo-emission and resonant photo-emission measurements from the α (monoclinic) and δ (FCC) allotropic phases of plutonium metal have been collected on beam line 7.0 at the ALS and the spectra show pronounced differences between the phases. The Pu $4f_{7/2}$ core level spectra obtained from both phases have sharp metallic features indicative of core hole shielding by de-localised electrons. However, the screening is enhanced in the α-Pu spectrum and suggests a larger degree of de-localisation than in δ-Pu. The results from the resonant valence band photo-emission measurements show greater spectral enhancement from the δ-Pu than the α-Pu, which is also consistent with a greater degree of localisation in δ-Pu.

One specific consequence of third-generation VUV/soft X-ray SR source development is the renaissance of XES techniques. XES is an atom specific probe, complementary to both photo-emission and absorption, that is especially amenable to studies of buried, disordered and bulk materials systems. Thus, XES is well suited for characterising the electronic properties of actinide materials since complications with surface contamination and sample preparation can be avoided. Results from XES

studies can be interpreted within existing theoretical frameworks. The results from XES investigations of the uranium oxides materials will be presented. A significant amount of information about actinide materials chemistry and physics can be obtained from a comprehensive multi-technique approach in the VUV/soft X-ray energy region that will lead to an improved understanding of the unique properties of these materials.

Acknowledgements

This work is supported by the Director, US Department of Energy, Office of Science, Office of Basic Energy Sciences, Chemical Sciences Division and Materials Sciences Divisions at LBNL and the ALS under contract No. DE-AC03-76SF00098.

RECENT ACHIEVEMENTS IN MULTI-KEV X-RAY MICROSCOPY

J. Susini, R. Barrett, M. Salomé and B. Kaulich
European Synchrotron Radiation Facility
BP 220, F-38043 Grenoble Cedex, France

Abstract

X-ray microscopy (XRM) techniques are emerging as powerful and complementary tools for sub-micron investigations. Soft XRM traditionally offers the possibility to form direct images of thick hydrated biological material in near-native environments, at a spatial resolution well beyond that achievable with visible light microscopy. Natural contrast is available in the soft X-ray region, in the so-called "water-window", due to the presence of absorption edges of the major constituents (C,N,O). Recent advances in manufacturing techniques have enlarged the accessible energy range of micro-focusing optics and offer new applications in a broad range of disciplines. XRM in the 1-20 keV energy range is better suited to map trace elements in fluorescence yield, 3-D tomographic imaging and in micro-diffraction. After a brief introduction to the principles and methods, the main attributes of X-ray microscopy will be presented. This presentation will be biased towards sub-micron microscopy developed at the ESRF in the 2-10 keV energy. Strengths and weaknesses of X-ray microscopy and spectromicroscopy techniques will be discussed and illustrated by examples in biology, materials sciences and geology.

For a complete review on X-ray microscopy see the following:

- "X-Ray Microscopy", G. Schmahl and D. Rudolf, eds., Springer, Berlin (1984).
- "X-Ray Microscopy II", D. Sayre, M. Howells, J. Kirz, and H. Rarback, eds., Springer, Berlin (1988).
- "X-Ray Microscopy III", A.G. Michette, G.R. Morrison, C.J. Buckley, eds., Springer, Berlin, (1992).
- "X-Ray Microscopy IV", V.V. Aristov and A.I. Erko, eds., Bogorod-skii Pechatnik, Moscow, (1994).
- "X-Ray Microscopy and Spectroscopy", J. Thieme, *et al*., eds., Springer, Berlin (1998).

More specific applications are developed in the followings references:

- J. Kirz, C. Jacobsen and M. Howells, *Quat. Rev. Biophys*., 28, 33 (1995).
- G. Schneider, *Ultramicroscopy*, 75, 85 (1998).

- G. Schneider, T. Schliebe and H. Aschoff, *J. Vac. Sci. Technol*., B 13, 2809 (1995).
- S. Spector, C. Jacobsen and D. Tennant, *J. Vac. Sci. Technol*., B 15, 2872 (1997).
- D. Weiss, M. Peuker and G. Schneider, *Appl. Phys. Lett*., 72, 1805 (1998).
- B. Kaulich, *et al*., *Appl. Phys. Lett*., 75, 4061 (1999).
- W. Yun, *et al., Rev. Sci. Instrum*., 70 (9), 3537 (1999).
- E. Di Fabrizio, F. Romanato, M. Gentili, S. Cabrini, B. Kaulich, J. Susini and R. Barrett, *Nature*, 401, 895 (1999).
- J. Kirz and H. Rarback, *Rev. Sci. Instrum*., 56 (9), 1 (1985).
- G. Schmahl, D. Rudolph, P. Gutmann and O. Christ, *Quat. Rev. Biophys*., 13, 293 (1980).
- H. Ade, X. Zhang, S. Cameron, C. Costello, J. Kirz and W. Williams, *Science*, 258, 872 (1992).
- C. Buckley, N. Khaleque, S.J. Bellamy, M. Robins, X. Zhang, in Ref.[1], II-47 (1998).
- P. Dhez, P. Chevallier, T.B. Lucatorto and C. Tarrio, *Rev. Sci. Instrum*., 70 (4), 1907 (1999).

EXAFS INVESTIGATION OF U(VI) INTERACTION WITH BACTERIA

C. Hennig, P.J. Panak,* T. Reich, J. Raff, S. Selenska-Pobell,
A. Roßberg, H. Funke, M.L. Merroun, G. Bernhard
Forschungszentrum Rossendorf e.V., Institute of Radiochemistry
P.O. Box 510119, D-01314 Dresden, Germany

Abstract

Bacteria in soil, sediment and water have a significant influence on the transport of radionuclides and other heavy metals in nature. Certain bacterial strains can selectively accumulate various metal ions from aqueous systems [1] and are, therefore, important for the regulation of environmental pollution and remediation. Because of the high resistance of their spores to extreme conditions, bacilli are found in a large variety of natural habitats. Recently, it was demonstrated that two *Bacillus* strains, *B. cereus* JG-A30 and *B. sphaericus* JG-A12, recovered from a uranium mining waste site in Germany, are able to accumulate selectively a large variety of heavy metals from the drain waters of the waste site [2]. In particular, it was shown that these strains accumulate large amounts of uranium.

Uranium(VI) complex formation at vegetative cells and spores of *Bacillus cereus* and *Bacillus sphaericus* was studied using uranium L_{II}-edge and L_{III}-edge extended X-ray absorption fine structure (EXAFS) spectroscopy. A comparison of the measured equatorial U-O distances and other EXAFS structural parameters of uranyl complexes formed at the *Bacillus* strains with those of the uranyl structure family indicates that the uranium is predominantly bound as uranyl phosphate [3].

* Current address: Lawrence Berkeley National Laboratory, MS 70A-1150, Berkeley, CA 94720, USA.

REFERENCES

[1] S. Selenska-Pobell, P. Panak, V. Miteva, I. Boudakov, G. Bernhard, H. Nitsche, "Selective Accumulation of Heavy Metals by Three Indigenous *Bacillus* Strains, *B. cereus*, *B. megaterium* and *B. sphaericus*, from Drain Waters of a Uranium Waste Pile", *FEMS Microbiol. Ecol*., 29, 59-67 (1999).

[2] P.J. Panak, J. Raff, S. Selenska-Pobell, G. Geipel, G. Bernhard, H. Nitsche, "Complex Formation of U(VI) with *Bacillus*-isolates from a Uranium Mining Waste Pile", *Radiochim. Acta*, in press.

[3] C. Hennig, P.J. Panak, T. Reich, A. Roßberg, J. Raff, S. Selenska-Pobell, W. Matz, J.J. Bucher, G. Bernhard, H. Nitsche, "EXAFS Investigation of Uranium(VI) Complexes Formed at *Bacillus cereus* and *Bacillus sphaericus* Surfaces", *Radiochim. Acta*, submitted.

SPECIATION OF THE ACTINIDE HUMATE COMPLEXATION BY XAFS

Melissa A. Denecke,* Kathy Dardenne, Christian M. Marquardt, Jörg Rothe
Forschungszentrum Karlsruhe, Institut für Nukleare Entsorgung
P.O. Box 3640, D-76021 Karlsruhe, Germany
*melissa@ine.fzk.de

Mark P. Jensen
Argonne National Laboratory, Chemistry Division
9600 S. Cass Avenue, Argonne, IL 60439, USA

Abstract

EXAFS results from Hf(IV) and Th(IV) humates identify carboxylate groups as the primary humic acid (HA) binding sites for cations. EXAFS structural parameters obtained for Np(V) humate at pH = 7 show the same trend as those previously observed for U(VI) humates. Furthermore, the only measurable difference between the Np co-ordination in Np(V) humate at pH = 7 compared to pH = 9 is the presence of a Np-Np interaction near 3.84 Å. No changes in the first Np-O co-ordination sphere, which would be evidence for co-ordination of a OH ligand in a hydrolysed Np mixed colloid complex $(NpO_2(OH)HA)_{colloid}$, is observed. STXM images of HA colloids at pH = 4.4 show globular and rod-like agglomerates with diffuse contours. These diffuse contours disappear in images of mixtures of organic humic acid and inorganic clay colloids. In the mixtures, aggregates with distinct, fractal-like shapes are observed; no separate aggregation of HA occurs. The carbon *1s* NEXAFS spectrum of HA shows distinct peaks associated with $1s \rightarrow \pi^*$ transitions of C=C and C=O bonds.

Introduction

Establishing the role that humic colloid mediated actinide transport plays in immobilisation and mobilisation processes in the environment is prerequisite to the successful development of performance assessment modelling codes. To this end, actinide-humic colloid interactions must be understood. The most important characteristic endowing humic substances (HS) potential as an avenue for colloid-mediated radionuclide transport is their strong complexing ability for cations. Various experimental approaches are and have been implemented to speciate actinide cations in the presence of HS. In this paper, the primary interaction of humic acid (HA) with Np(V), Th(IV) and Hf(IV), as a tetravalent actinide homologue, are determined by comparing structural parameters of the metal cation co-ordination in their humate complexes with either previous results or with a reference system. Structural, metrical parameters are extracted from the L3 edge extended X-ray absorption fine structure (EXAFS) spectra. The effect of increasing the pH from 7 to 9 on the structure of the actinide co-ordination sphere for the Np(V) humate is also studied. The colloidal, macromolecular HS structure and changes affected by the presence of mineral colloids are determinant in the ability of humic colloids to mediate actinide transport. For this reason, the tertiary structure of HA colloids alone and in association with mineral colloids are determined from their scanning transmission X-ray microscopic (STXM) images. The C *1s* edge near-edge X-ray absorption fine structure (NEXAFS) of HA is compared to that of carboxylated latex spheres in order to identify absorption features in the spectrum. Despite the advantages of approximately a tenfold higher resolution over light microscopy, the possibility of measuring in solution that other microcroscopies do not offer and the supplemental spectroscopic, chemical information that STXM offers, only few reports of its application to studies of natural organic material have appeared in the literature [1-3].

EXAFS investigation on the interaction of Hf(IV) and Th(IV) with HA and Bio-Rex70

EXAFS investigations of U(VI) sorbed onto HA showed the structural parameters for the U(VI) co-ordination to be invariant of HA type, preparation conditions and cation loadings [4]. This suggests that the same HA functional groups are responsible for binding U(VI). According to IR results and the pH applied for sample preparation, these functional groups are carboxylate groups. Noteworthy is that a U(VI)-HA prepared using a synthetic HA also exhibited the same co-ordination, despite having a much higher phenolic OH:carboxylate group ratio than the other HA investigated [4,5]. This indicates that the HA phenolic OH groups play a subordinate role compared to carboxylate groups in complexing U(VI).

In order to test the hypothesis that HA carboxylate groups are generally responsible for binding metal cations, co-ordination numbers (N), bond distances (R) and Debye-Waller factors (σ^2) of Hf(IV) and Th(IV) sorbed onto HA are determined from their metal L3 EXAFS spectra. These are compared to those found for Hf(IV) and Th(IV) sorbed onto Bio-Rex70, a cation exchange resin having solely carboxylate groups [6]. If the HA carboxylate groups are responsible for complexing the metal cations, while HA phenolic OH groups are unimportant, then the structural parameters for Hf(IV) and Th(IV) sorbed onto HA should be the same as those exhibited by these metal cations sorbed onto Bio-Rex70.

All sorption samples are prepared from 250±1 mg either purified HA (Aldrich) or protonated Bio-Rex70 (Bio-Rad) suspended in approximately 35 mL 0.1 M $HClO_4$. Following adjustment of pH to ~2 with NaOH, 5 mL of a 0.1 M $HClO_4$ solution containing 29.5 mM Hf(IV) or 26.2 mM Th(IV) are added and the pH readjusted to ~1.6. The resulting volume of the reaction solution is near 50 mL. The solution is stirred for 66-68 h, at constant pH 1.63±0.05, under ambient conditions. The sample is isolated by centrifugation, washing once with 50 mL Milli-Q water. The quantity Hf(IV) or Th(IV) sorbed is determined as the difference between the initial and supernatant concentrations. The Hf(IV)

loading onto HA and Bio-Rex70 is 86 mg/g and 15 mg/g, respectively. With a proton exchange capacity (PEC) of 5.43 mEq/g for Aldrich HA [7] and 10.2 mEq/g for Bio-Rex70 and assuming charge neutralisation, these loadings are equivalent to 35% PEC and 3% PEC. The corresponding Th(IV) loadings are 128 mg/g HA and 41 mg/g Bio-Rex70, which is equivalent to 41% PEC and 7% PEC, respectively.

For EXAFS measurements, a portion of each sample was placed in wet paste form into a capped 400 μL polyethylene (PE) centrifuge tube. The rest of the sample was air-dried, dispersed in PE powder and pressed as 1.3 cm diameter pellets. In addition to the sorption samples, polycrystalline tetrakis-acetylacetonate hafnium(IV), $Hf(acac)_4$ and bis(tetraethylammonium) hexanitrato-thorium(IV), $[(C_2H_5)_4N]_2Th(NO_3)_6$, are also studied as pressed PE pellets.

EXAFS spectra were recorded on the Hf and Th L3 edges, at room temperature, in transmission mode, at the Hamburger Synchrotronstrahlungslabor (HASYLAB) on beam line A1. A Si(311) double-crystal monochromator, detuned 50% of the maximum incident flux, was used. Hafnium L3 edge spectra were calibrated against the first inflection point in the K edge of a Zn foil defined as 9 660.8 eV. L3 edge spectra of the Th samples were calibrated in a similar manner using the K edge of a Y foil defined as 17 038.0 eV.

The L3 electron ionisation energy, E_0, for all Hf samples was defined as 9 565.0 eV; E_0 was defined as 16 315 eV for Th samples. Averaged spectra of two or more scans for each sample were analysed using the suite of programs EXAFSPAK [8]. Theoretical oxygen backscattering amplitude and metal-oxygen phase-shift functions applied during fits to the data are calculated using FEFF7 [9] for a 29 atom cluster using either atomic positions for $Hf(acac)_4$ [10] or those for $[NH_4]_2Th(NO_3)_6$ [11]. The error associated with the bond length determination with the EXAFS method for these samples, as well as for the Np humates reported in the next section, is ±0.02 Å; the error for co-ordination number is ±20% [12].

The k^3-weighted Hf and Th L3 edge spectra and their corresponding Fourier transforms (FT) are shown in Figure 1. Visual inspection of the spectra reveals that the EXAFS pattern for all Hf(IV) sorption samples is nearly the same in HA and Bio-Rex70 samples, but different from that of the polycrystalline reference compound. The same is true for the Th(IV) samples.

The back-transformed first peak in the FT of each spectrum was fit to the EXAFS equation using oxygen atoms as backscatterers. Fit results are listed in Table 1. The excellent agreement between N and R from EXAFS fits and XRD results for the two polycrystalline compounds substantiates the "correctness" of theoretical phase and amplitude functions used. For both Hf(IV)-HA and Hf(IV)-Bio-Rex70, in wet paste and air-dried forms, approximately 6-7 oxygen atoms at R = 2.14 Å are found. Both Th(IV)-HA and Th(IV)-Bio-Rex70 exhibit 9-10 oxygen atoms at 2.43 Å.

Because similar structural parameters for metal cation sorption onto both HA and Bio-Rex70 are found, it is assumed that the same type of complexation occurs in both systems. Because Bio-Rex70 only has carboxylate groups capable of cation binding, having the same complexation implicates carboxylate groups responsible for cation binding in HA. If a significant number of HA functional groups other than carboxylate groups were involved, e.g. phenolic OH groups, then interatomic distances would be different and an EXAFS pattern unlike that of their Bio-Rex70 counterparts would be expected. For example, there is a difference greater than 0.18 Å between U-O distances associated with co-ordinated phenol and co-ordinated carboxylate for the salicylate complex reported in [13].

Figure 1. k^3-weighted Hf (top) and Th (bottom) L3 edge EXAFS (left) and their corresponding Fourier transforms (right) for the Hf(IV) and Th(IV) sorption samples (H stands for HA, B for Bio-Rex70 and P for wet paste sample), $Hf(acac)_4$ and $[(C_2H_5)_4N]_2Th(NO_3)_6$

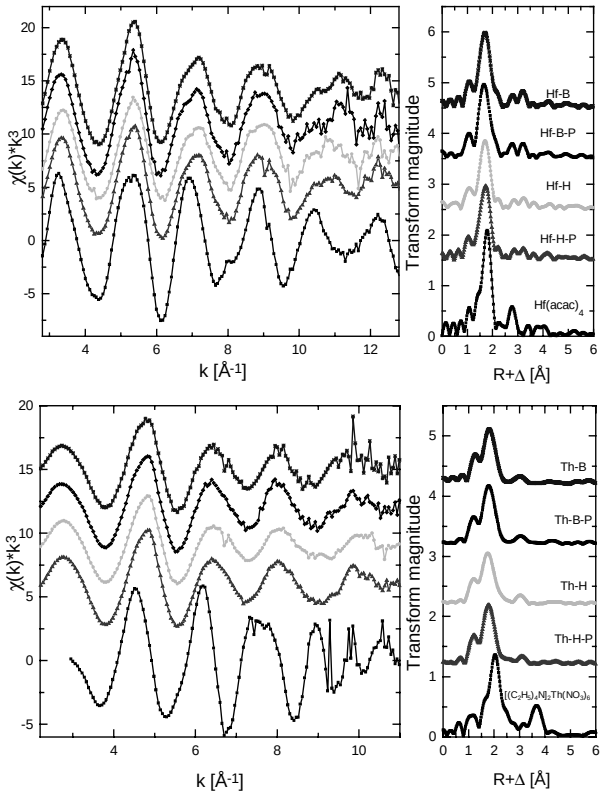

Table 1. Fit results to Fourier-filtered first oxygen shell Hf (top) and Th (bottom) L3 edge EXAFS. ΔE_0 was held constant at 8 eV for the Hf sorption samples and at 1 eV for the Th sorption samples.

Sample	**Hf-HA**	**Hf-HA paste**	**Hf-Bio-Rex70**	**Hf-Bio-Rex70 paste**	**$Hf(acac)_4$**
N	5.8	6.7	7.3	7.4	8.1 (8)*
R [Å]	2.13	2.14	2.14	2.15	2.18 (2.199)*
σ^2 [Å^2]	0.007	0.007	0.009	0.009	0.006
Sample	**Th-HA**	**Th-H paste**	**Th-Bio-Rex70**	**Th-Bio-Rex70 paste**	**$[(C_2H_5)_4N]_2Th(NO_3)_6$**
N	9.9	10.1	9.4	9.4	12.1 (12)*
R [Å]	2.43	2.43	2.44	2.44	2.57 (2.565)*
σ^2 [Å^2]	0.015	0.013	0.013	0.012	0.007

* Values in parentheses are those calculated from the XRD crystal structure determination by for $Hf(acac)_4$ [10] and for $[(C_2H_5)_4N]_2Th(NO_3)_6$ [11].

Results from IR and XPS investigations of the same samples corroborate these conclusions. Observed changes in IR spectra of the HA before and after treatment with Hf(IV) involve bands associated with vibrations of carboxylate groups. XPS measurements in vacuum are considered feasible because EXAFS results are essentially the same for wet paste and dried samples. The XPS results show that *4f*-binding energies for Hf(IV) or Th(IV) sorbed onto HA are identical to that for the corresponding Bio-Rex70 sample. In addition, the $4f_{7/2}$ and $4f_{5/2}$ lines for both HA and Bio-Rex70 sorption samples can be fit with single curves, pointing to a single type of interaction. This information confirms that Hf(IV) and Th(IV) are sorbed primarily onto HA carboxylate groups; other HA functional groups play, at most, a secondary role in metal cation sorption.

Np L3 edge EXAFS studies on Np(V) complexed with HA

Previous investigations using optical spectroscopy on NpO_2^+ humates show changes in Np speciation in samples at pH = 7 compared to samples at pH = 9 [14]. This is associated with a near four-fold increase in the loading capacity (LC) of the HA. The increase is larger than the linear increase in LC with pH observed for other cations [15]. At pH = 9 for Np(V) concentrations used in [14], NpO_2^+ is known to be partially hydrolysed and spectroscopic results are interpreted as a formation of a mixed hydrolysed NpO_2^+ hydroxo-humate colloid complex, $(NpO_2(OH)HA)_{colloid}$. Thus, EXAFS investigations are performed on the Np L3 absorption edge of aqueous solutions of Np(V) and HA at pH = 7 and 9 in order to elucidate Np(V)-HA structural changes associated with the observed speciation change going from pH = 7 to 9.

The samples are made from 2 mL of two HA (purified Aldrich) stock solutions, both with concentrations near 10 g HA/L but different pH (~7 and 9), and 60 µL 36 mM Np(V) stock solution in 1 M $HClO_4$. Samples are prepared in a N_2-purged box. The pH is readjusted following addition of the Np(V) by adding 20 µL 1 M NaOH and then 40 µL or 60 µL 0.2 M NaOH to obtain a pH of 6.99 or 9.04, respectively. Based on published values for the HA PEC (5.43 mEq/L [7]), log β (3.58 [14]), and loading capacity (13% at pH = 7 and 43% at pH = 9 [14]), the amount of Np(V) and HA in the samples provides 25 and 93 times more complexed Np(V)-HA than free Np(V) in solution at pH = 7 and pH = 9, respectively. The optical absorption spectra of the Np(V)-HA solutions show an absorption maximum at 990 nm for the pH = 7 sample and 992 nm for the pH = 9 sample; no absorption peak for free Np(V) aquo species at 980 nm is observed. Aliquots of these solutions are placed in 5 mm × 10 mm Plexiglas cuvettes for the EXAFS measurements. The solutions are contained within the cuvette by a plastic plug insert, which is sealed with two layers of epoxy, having absorbent sandwiched between them, and covering with another plastic stopper. The cuvettes are mounted in the Argonne Actinide Facility multiple sample changer [16] so that a 10 mm path is directed towards the incident beam.

XAFS measurements are performed at the Advanced Photon Source (APS), BESSRC beam line 12BM, using a Si(111) double-crystal monochromator. The 12BM beam line is equipped with a collimating and focusing mirror. The beam spot used is 0.5 mm^2. The incident beam is free of higher harmonic reflections, as is shown by the absence of the corresponding inelastic scattering peaks recorded with an energy dispersive detector. The spectra are calibrated by defining the first inflection point of the first derivative XANES spectrum of a Zr foil as 17 998 eV, which is recorded at the beginning of the XAFS measurements and again at the end. The energy shift between both measurements is less than the smallest step size in the spectra recorded, 0.5 eV. Spectra are collected in both transmission mode and fluorescence mode. Data reduction and analysis is performed using the WinXAS program [17]. The single scattering backscattering amplitude and phase-shift functions used in the analysis are calculated with the theoretical EXAFS modelling code FEFF8 [18]. E_0 is defined as 17 613 eV for both spectra.

The k^3-weighted Np L3 edge transmission EXAFS spectra of both Np(V) humate samples is depicted in Figure 2. There is little difference between the oscillatory pattern exhibited by the two samples. The Fourier filtered nearest-neighbour oxygen co-ordination shells for the pH = 7 sample fluorescence spectrum is fit to the EXAFS equation using a model with two oxygen co-ordination shells. The structural metrical parameters for the oxygen atoms belonging to the trans-dioxo neptunyl moiety are $N_{ax} = 2$ (held constant during the fit procedure), $R_{ax} = 1.83$ Å and $\sigma^2_{ax} = 0.001$ Å^2. Parameters for the equatorial oxygen atoms are $N_{eq} = 5.3$, $R_{eq} = 2.47$ Å and $\sigma^2_{eq} = 0.006$ Å^2. ΔE_0 is set as a global parameter for both shells and 13.8 eV is obtained in the fit. The ΔR value calculated from the beat-node [19] located at k = 7.38 Å^{-1} in the oscillatory pattern of the Fourier filtered data yields $\Delta R_{(beat\text{-}node)} = 0.639$ Å. This is in agreement with the difference between R_{ax} and R_{eq} obtained in the fit: $\Delta R_{(fit)} = 0.64$ Å. The Np(V) humate average equatorial oxygen bond length is somewhat shorter than that observed for the Np(V) aquo species: 2.47 Å versus 2.50 Å [20], respectively. This slight shortening of the average equatorial bond lengths is similar to the trend observed for U(VI). A decrease from 2.42 Å in the U(VI) aquo species [21] to $R_{eq} = 2.38$ Å following U(VI) complexation to humic acid [4] is observed.

Figure 2. Right: k^3-weighted Np L3 edge EXAFS for Np(V):HA at pH = 7 and pH = 9 (above) and their difference spectrum (below). Left: the corresponding FT of the EXAFS at right. FT range = 3.6-14.3 Å, using a Bessel window.

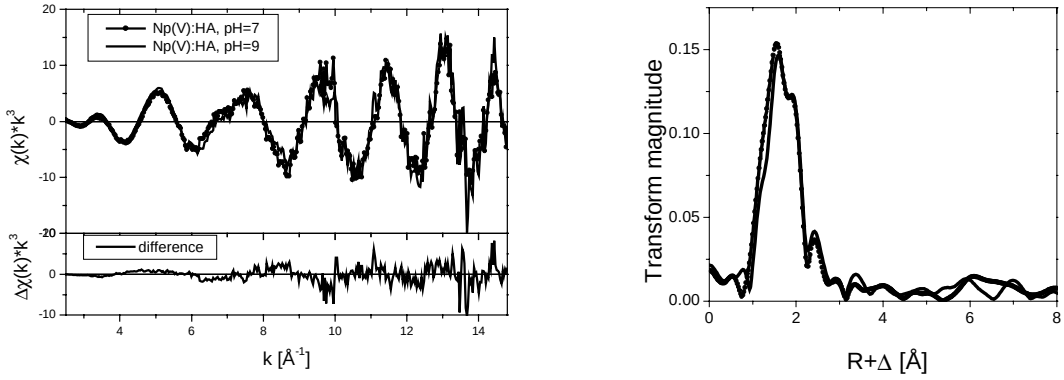

Because the two spectra are very similar, their difference spectrum is calculated in order to ascertain any change in structure between the Np(V) humate sample at pH = 7 and pH = 9. The difference spectrum shown in Figure 2 is not simply a residual but exhibits an oscillatory pattern, indicative of an associated backscattering co-ordination shell. The Fourier transform of the difference spectrum shows a peak intensity near 3.7 Å. This peak is isolated by backtransforming it to k-space. The filtered oscillation is then fit to the EXAFS equation. The phase and amplitude of this oscillation can be modelled using a Np-Np interaction. The result is shown in Figure 3. The structural parameters for this Np-Np interaction are $N_{Np} = 0.96$, $R_{Np} = 3.84$ Å, and $\sigma^2_{Np} = 0.0024$ Å^2. Attempts to model this peak with other nearest neighbour distances feasibly present at distances ~4 Å, such as a distal oxygen belonging to a co-ordinating carbonate ligand, are unsuccessful.

The EXAFS results do not explicitly substantiate the formation of a hydrolysed mixed colloid complex $(NpO_2(OH)HA)_{colloid}$ from changes in the Np-O co-ordination that might indicate co-ordination of a OH ligand. The structural difference between the Np(V) humate species at pH = 7 and pH = 9 is the presence of a single Np-Np interaction at 3.84 Å. The amount of uncomplexed Np(V) in solution for these experiments is very low, so that the Np-Np interaction is not a solution hydrolysis species. The observed anomalous increase in the LC going from pH = 7 to 9 [14,15] may be due to interaction of polynuclear species with the humate.

Figure 3. k^3-weighted filtered EXAFS oscillations extracted from the difference spectrum shown in Figure 2 and the theoretical EXAFS for the Np-Np interaction obtained as fit result

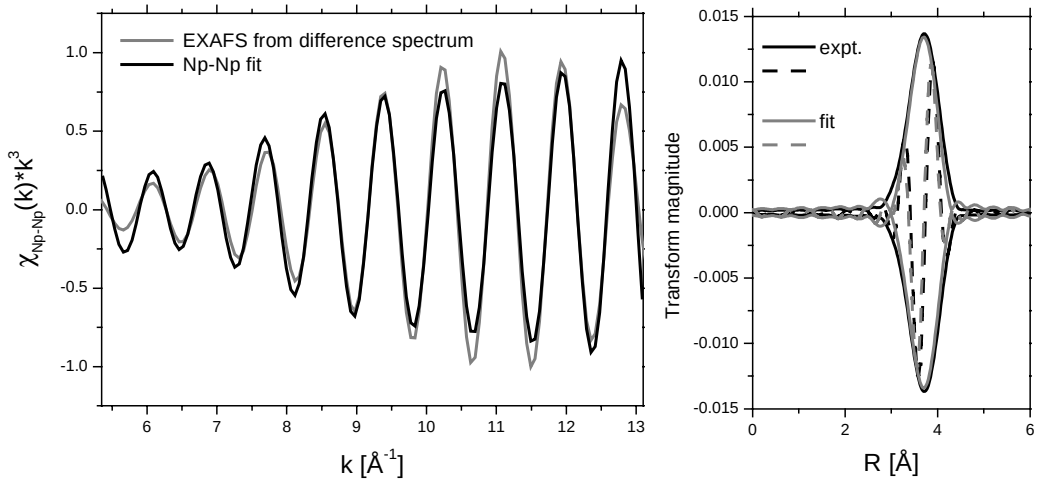

Soft X-ray spectromicroscopy of aquatic HA and clay colloid mixtures

In situ STXM images of aqueous suspensions of mixed mineral-organic colloids are recorded as a function of colloid type. The aim of these experiments is to establish, under defined conditions, whether truly mixed agglomerates form, whether the colloids cluster separately or whether an organic coating on the mineral colloid surfaces occurs. The exact nature of this interaction will effect the colloid's sorption behaviour for actinide ions. Images of aqueous suspensions of HA (0.2 mg/mL, I = 0.1 M NaCl, pH = 4) of mixtures of montmorillonite and HA (0.1 mg HA/mL, 0.21 mg clay/mL, pH = 5.8), as well as montmorillonite mixed with polystyrene (PS) latex particles (0.23 mg PS/mL, 0.21 mg clay/mL, pH = 6.8), which have been chemically modified to have a carboxylated surface, are presented. By comparing micrograph images recorded at photon energies above and below the C *1s* X-ray absorption edge, the organic components can be differentiated from inorganic components. Comparison of the HA C *1s*-NEXAFS spectra, extracted from image stacks recorded while incrementally increasing the photon energy, to that recorded for the reference latex colloids is also made.

Purified Aldrich HA, surfactant-free carboxyl polystyrene latex particles (400±8 nm diameter according to TEM, surface charge content 11.7 μEq/g, Interfacial Dynamics) and the calcium montmorillonite Ibeco, size fractioned by sedimentation [22] (Bentonit Technologie) are the materials used. The polystyrene latex with carboxylated surfaces is chosen as a reference sample because it is a suitable size standard and because the carboxylated surface should chemically mimic HA.

Aqueous colloid suspensions are sandwiched as a few μm thick film, held between Si_3N_4 membranes of 100 nm thickness by capillary forces, using a wet cell assembly to maintain the samples in a hydrated state for several hours [23]. The presence of persisting hydrated conditions in the wet cell throughout the time span of recording image stacks is confirmed by the observation of an edge of the water film after final images are recorded.

STXM investigations are performed at the National Synchrotron Light Source X1A end station, operated by the State University of New York at Stony Brook [24]. A Fresnel zone plate of 160 μm diameter and 45 nm outer ring segment width is used to focus the soft X-rays. The energy of the spherical grating monochromator is calibrated relative to the C *1s*-threshold resonance of CO_2 at

290.74 eV [25]. The C *1s*-NEXAFS spectra are obtained from 62 image stacks recorded between about 275 eV and 310 eV. The energy range is divided into three regions: 275-283 eV in 1 eV steps, 283-290 eV in 0.2 eV steps and 290-309 eV in 1 eV steps. A linear pre-edge background was subtracted from the resulting spectra, followed by normalisation (μ*d = 1) at 300 eV. For a review of the image stack data analysis, see [26].

A STXM image of a large HA agglomerate is shown in Figure 4. The HA macromolecular agglomerates observed in the micrographs exhibit only diffuse contours at dimensions in the μm range. Both globular (spherical-to-elliptical) as well as filament-type particle aggregates were observed. The absorption contrast in the images recorded above and below the C *1s* edge show that these diffuse contoured areas are zones of high carbon concentration and are therefore HA. The HA C *1s*-NEXAFS spectrum extracted from a 1 μm × 4 μm area of high absorption at 290 eV is shown in Figure 5.

Figure 4. STXM image (290 eV) of hydrated HA aggregates at pH = 4

Magnification = 2 800 ×

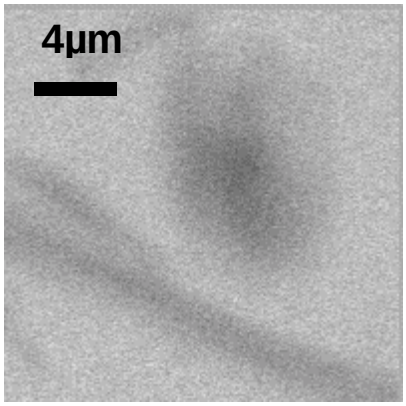

Figure 5. Normalised C *1s*-NEXAFS of carboxylated polystyrene microspheres (top), HA (bottom)

Absorption transitions marked A and B correspond to a 1s→π (C=C) and a 1s→π* (C=O) transition, respectively*

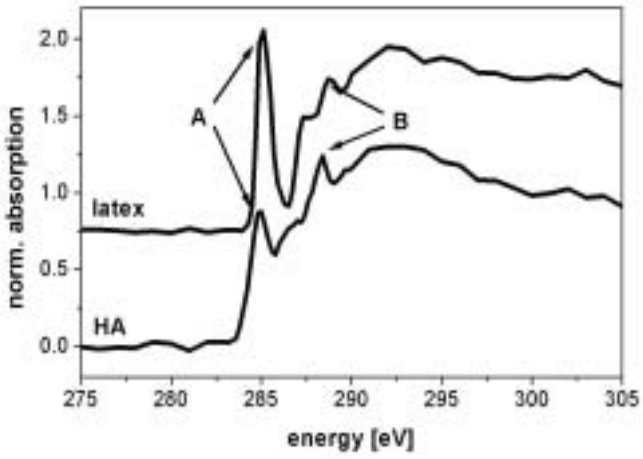

Images at 20×20 µm^2 of montmorillonite + PS suspension are shown in Figure 6 recorded below and above the C K edge. The left image appears to be brighter due to carbon deposits on optical elements such as mirrors and gratings. Clay mineral particles are visible in the left image as dark and diffuse patches due to their unspecific absorption at 281.8 eV. The polystyrene latex microspheres are clearly enhanced in the right image due to their strong C *1s* absorption at 290.7 eV. Comparison of both images shows that the latex spheres tend to cluster near or around clay mineral particles. However, there is no evidence that the presence of the latex spheres influences the structure or the arrangement of the mineral particles. The C *1s*-NEXAFS spectrum extracted from a near 1.5 µm^2 area of clustered PS spheres in an image stack are shown in Figure 5.

Figure 6. STXM images of a montmorillonite + PS suspension measured below (left, 281.8 eV) and above (right, 290.7 eV) the C *1s* edge

Magnification = 2 700 ×

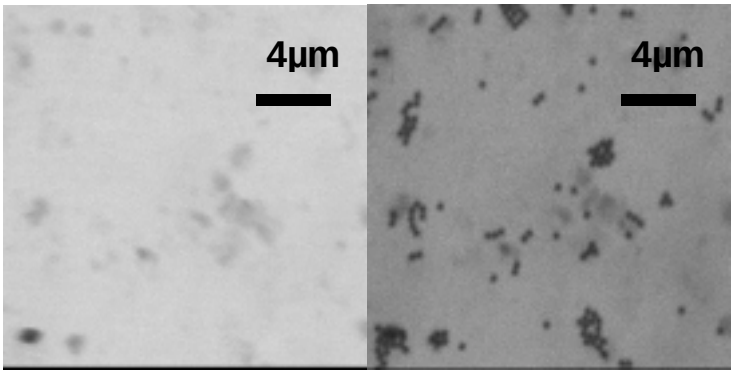

Clustering of HA on or near montmorillonite also occurs in the mixed HA + clay suspensions (Figure 7). However, in this case the diffuse-contoured HA morphology is not observed. STXM images show a specific form of aggregation of the clay particles induced by the presence of HA. Fractal-like structures of colloid aggregates are detected with HA having remarkably sharp contours. This corroborates previous X-ray microscopy results reported by Myneni, *et al*. [2], that the presence of minerals dramatically alters the humic substance macromolecular structure in aqueous solutions.

Figure 7. STXM images of montmorillonite + HA recorded at 275.5 eV (left) and 285.2 eV (right)

Magnification = 1 600 × (top), 300 × (bottom)

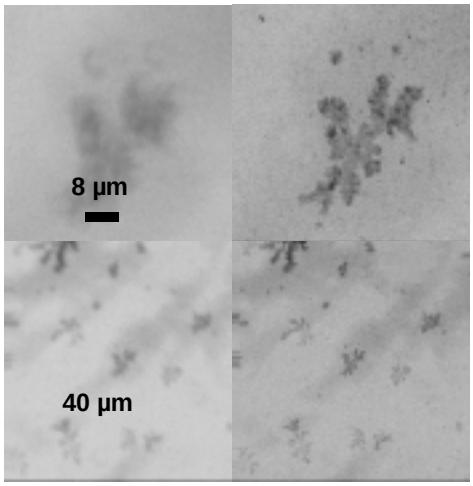

The general similar affinity of both the carboxylated PS particles and the HA colloids for the clay in the organic/inorganic mixed suspensions suggests a similar interaction in both systems. Because the PS surface carboxyl groups are presumed responsible for their affinity for the clay colloids, it is likely that HA carboxyl groups are also responsible for the HA affinity for the clay particles. The different aggregate morphologies for the two mixed colloid suspensions results from the rigidity of the PS microspheres, whereas HA has a dynamic macromolecular conformation allowing it to unfold and spread onto the clay surface.

Conclusions

The EXAFS investigation of the interaction of Hf(IV) and Th(IV) with HA and Bio-Rex70 supports the hypothesis that these metal cations are sorbed primarily onto HA carboxylate functional groups. Similar results are reported for the complexation of U(VI) with HA [4]. This may allow significant simplification of models used to predict radionuclide migration via HA-mediated transport in the hydro and geosphere. Comparison of EXAFS results from Np(V)-HA at pH = 7 with the Np(V) aquo species shows the cation-humate interaction to be similar to that previously reported for the actinyl U(VI) interaction with HA [4]. Polynuclear Np(V) sorption onto HA at pH = 9 is likely the cause for the observed anomalous LC increase at higher pH values for this cation [14,15]. Results from STXM images of mixed organic-inorganic colloids may explain previously reported observations that the presence of HA is found to mask the complexation behaviour of mineral colloids for actinide cations [27,28]. The aggregation of clay and HA, which appear to coat the clay surface, would expectedly exhibit a different sorption behaviour than that for the colloids separately. Furthermore, if conditions are such that the agglomeration/coating is great, then modelling of the actinide cation interaction with the agglomerates in solution may, in some cases, simplify to ascertaining the number of potential complexing surface groups available. By following variations in the HA C *1s*-NEXAFS features upon complexation of actinide cations to HA alone and in mixed colloid systems, it may be possible to identify functional groups responsible for the complexation.

Acknowledgements

HASYLAB, the BESSRC CAT at APS and Professor Dr. C. Jacobsen (NSLS) are gratefully acknowledged for beam time allotment. The Ibeco montmorillonite was kindly provided by Dr. A. Bauer. Use of the infrastructures of the Actinide Facility for synchrotron research in the Chemistry division of Argonne National Laboratory (ANL) is also acknowledged with gratitude. A portion of the work at ANL was supported by the US Department of Energy, Basic Energy Sciences, under contract No. W-31-109-ENG-38.

REFERENCES

[1] J. Rothe, M.A. Denecke, K. Dardenne, *J. Colloid Interface Sci*., 231, 91-97 (2000).

[2] S.C.B. Myneni, J.T. Brown, G.A. Martinez, W. Meyer-Ilse, *Science*, 286, 1335 (1999).

[3] J. Thieme, J. Niemeyer, *Progr. Colloid Polym. Sci*., 111, 193 (1998).

[4] M.A. Denecke, S. Pompe, T. Reich, H. Moll, M. Bubner, K.H. Heise, R. Nicolai, H. Nitsche, *Radiochim. Acta*, 79, 151-159 (1997).

[5] S. Pompe, M. Bubner, M.A. Denecke, T. Reich, A. Brachmann, G. Geipel, K.H. Heise, H. Nitsche, *Radiochim. Acta*, 74, 135-140 (1996).

[6] M.A. Denecke, D. Bublitz, J.I. Kim, H. Moll, I. Farkes, *J. Synchrotron Rad*., 6, 394-396 (1999).

[7] J.I. Kim, G. Buckau, G.H. Li, H. Duschner, N. Psarros, *Fresenius J. Anal. Chem*., 338, 245-252 (1990).

[8] G.N. George, I.J. Pickering, "EXAFSPAK: A Suite of Computer Programs for Analysis of X-ray Absorption Spectra", Stanford Synchrotron Radiation Laboratory, Stanford, CA, USA (1995).

[9] S.I. Zabinsky, J.J. Rehr, A. Ankudinov, R.C. Albers, M.J. Eller, *Phys. Rev*., B52, 2995-3009 (1995).

[10] J.V. Silverton, J.L. Hoard, *Inorg. Chem*., 2, 243-249 (1963).

[11] M.R. Spirlet, J. Rebizant, C. Apostolidis, B. Kanellakopulos, E. Dornberger, *Acta Cryst*., C48, 1161-1164 (1992).

[12] "X-ray Absorption: Principles, Applications, Techniques of EXAFS, SEXAFS and XANES", D.C. Koningsberger, R. Prins, eds., John Wiley & Sons, New York (1988).

[13] L.R. Nassimbeni, A.L. Rodgers, J.M. Haigh, *Inorg. Chim. Acta*, 20, 149 (1976).

[14] C. Marquardt, J.I. Kim, *Radiochim. Acta*, 80, 129-137 (1998).

[15] "Effects of Humic Substances on the Migration of Radionuclides: Complexation and Transport of Actinides" (Final Report), EUR Report, G. Buckau, ed., in print.

[16] On the internet page http://chemistry.anl.gov/heavy-element/actinide/multiple.html, the cell is described.

[17] T. Ressler, *J. Physique IV*, 7, C2-269 (1997).

[18] A.L. Ankudinov, B. Ravel, J.J. Rehr and S.D. Conradson, *Phys. Rev*., B58 (12), 7565-7576 (1998).

[19] G. Martens, P. Rabe, N. Schwenter, A. Werner, *Phys. Rev. Lett*., 29, 1411-1414 (1977).

[20] P.G. Allen, J.J. Bucher, D.K. Shuh, N.M. Edelstein, T. Reich, *Inorg. Chem*., 36, 4676-4683 (1997).

[21] H.A. Thompson, G.E. Brown, G.A. Parks, *Amer. Mineral*., 82, 483-496 (1997).

[22] A. Bauer, G. Berger, *Applied Geochemistry*, 13, 905-916 (1998). A. Bauer, B. Velde, *Clay Miner*., 34, 259-276 (1999).

[23] U. Neuhäusler, S. Abend, C. Jacobsen, G. Lagaly, *Colloid Polym. Sci*., 277, 719 (1999).

[24] C. Jacobsen, S. Williams, E. Anderson, M.T. Browne, C.J. Buckley, D. Kern, J. Kirz, M. Rivers, X. Zhang, *Opt. Commun*., 86, 351 (1991).

[25] A.P. Hitchcock, D.C. Mancini, *J. Electron Spectroscopy*, 67, 1 (1994).

[26] Stack software manual in http://xray1.physics.sunysb.edu/~jacobsen/stack/ stack.html.

[27] T. Zuyi, C. Taiwei, D. Jinzhou, D. Xiong Xin, G. Yingjie, *Applied Geochemistry*, 15, 133 (2000).

[28] Th. Rabung, “Einfluss von Huminstoffen auf die Europium(III)-Sorption an Hämatit”, Doctoral Thesis, Universität Saarbrücken (1998).

EXAFS STUDY OF U(VI) COMPOUNDS: A NEW APPROACH TO DATA ANALYSIS

Yu.A. Babanov,[1,2] **T.Ye. Zayarnaya**[1]
[1]Institute of Metal Physics
GSP-170, Ekaterinburg, 620219, Russia
[2]Udmurt State University, Izhevsk, Russia
Babanov@imp.uran.ru

T. Reich, H. Funke
Forschungszentrum Rossendorf e.V., Institute of Radiochemistry
P.O. Box 510119, D-01314
Dresden, Germany

Abstract

The regularisation method is applied to determine three partial pair correlation functions (PCFs) from one EXAFS spectrum. The mathematical procedure is discussed and applied to the EXAFS analysis of $UO_2(HAsO_4) \times 4H_2O$.

The measurements were performed at the Rossendorf Beamline (ROBL) at the ESRF in Grenoble. The As K edge and the U L3–edge absorption spectra were recorded in transmission mode at temperatures of 41 K and 15 K, respectively. From the U L3-edge EXAFS spectrum, we obtain the PCFs of the pairs U-U, U-As and U-O and determine the structural parameters for the first and the second co-ordination shells of each pair. The PCFs of the pairs As-U, As-As and As-O are obtained from the As K-edge EXAFS spectrum.

Introduction

The extended X-ray absorption fine structure (EXAFS) technique is a very powerful tool for the structure determination in a wide range of materials [1]. In general, for simple systems, the Fourier transformation methods, ratio-cumulant method and non-linear least-square fitting are used.

The Fourier transformation method is a non-inverse procedure for the integral equation describing EXAFS data. Firstly, the kernel of this equation is not a simple sin-function but a more complex function. Secondly, the integration in k space is limited at both sides: at high k the limit is given by the decreasing amplitude of oscillations with increasing k, at low k the single-scattering approximation, which is only taken into account in the integral EXAFS equation, is not valid. Formally, the integral EXAFS equation after the Fourier transformation reduces to an equivalent equation in r space, which is necessary to solve. Least-square fitting is a very unstable method. There exists an infinite amount of solutions for one set of experimental data.

The regularisation method of the numerical solution of the Fredholm integral equation of the first kind has been shown to be an attractive method to solve ill-posed problems [2]. Nearly two decades ago, it was suggested to apply this method to EXAFS data analysis [3,4]. Up to now, this technique has only been applied to experimental data of one-component and binary systems.

In this paper we use the regularisation method to study multi-component systems. We determine three pair correlation functions (PCFs) using only one experimental spectrum.

Regularisation algorithm for determining the partial pair correlation functions

If the system consists of n elements, then $N = n(n + 1)/2$ partial pair correlation functions $g_{ij}(r)$ are needed to describe the atomic structure, where $g_{ij}(r)$ is the density of the probability to find a pair of atoms i and j at an interatomic distance r.

The EXAFS integral equation in single-scattering approximation is written as [3]:

$$k\chi_i(k) = 4\pi\rho_0 \sum_{j=1}^{n} c_j \int_0^{\infty} f_j(k,r) e^{-\frac{2r}{\lambda_i(k)}} \sin\left(2kr + \psi_{ij}(k,r)\right) g_{ij}(r) dr \qquad (1)$$

where $\chi_i(k)$ is the normalised oscillating part of the X-ray absorption spectrum, ρ_0 is the atomic density of the compound, c_j is the concentration of atoms j, $f_j(k,r)$ is the backscattering amplitude of the neighbouring atom j, $\psi_{ij}(k,r) = (2\delta_i(k) + \varphi_j(k,r) + \pi)$ is the total phase shift, $\delta_i(k)$ is the phase shift on the central atom i, $\varphi_j(k,r)$ is the phase shift on the neighbouring atom j and $\lambda_i(k)$ is the mean free path of the photoelectron. The functions $f_j(k,r)$, $\psi_{ij}(k,r)$ and $\lambda_i(k)$ are obtained from curved wave approximation calculations with the program FEFF-8 for the crystalline reference sample [5]. We consider the experimental data for the U L3-edge and the As K-edge absorption spectra of $UO_2(HAsO_4) \times 4H_2O$ compound (i = U, As) and neglect the contributions of U-H, As-H pairs (j = U, As, O).

We take into account that the solution:

$$g_{ij}(r) = 0 \text{ at } r \le a_j \qquad (2)$$
$$g_{ij}(r) = 1 \text{ at } r \le b_j$$

where $a_j = r_i + r_j$ is the sum of neighbouring atoms radii and $b_j >> a_j$, and rewrite the integral EXAFS Eq. (1) in a symbolic form:

$$u_i = \sum_{j=1}^{n} A_{ij}\ g_{ij} \tag{3}$$

Here:

$$u_i(k) = \frac{k\chi_i(k)}{f_0(k)} - t_i(k) \tag{4}$$

and:

$$t_i(k) = 4\pi\rho_0 \sum_{j=1}^{n} c_j \int_b^{\infty} \frac{f_j(k,r)}{f_0(k)} \exp\left(-\frac{2r}{\lambda_i(k)}\right) \sin\left(2kr + \psi_{ij}(k,r)\right) dr \tag{5}$$

$$f_0(k) = \sum_{j=1}^{n} c_j\, f_j(k,b_j) \tag{6}$$

$f_0(k)$ is the average backscattering amplitude on the neighbouring atoms j.

The integral operator A_{ij} is defined as:

$$A_{ij}\, g_{ij} = 4\pi\rho_0 c_j \int_{a_j}^{b_j} \frac{f_j(k,r)}{f_0(k)} \exp\left(-\frac{2r}{\lambda_i(k)}\right) \sin\left(2kr + \psi_{ij}(k,r)\right) g_{ij}(r)\, dr \tag{7}$$

After discrete approximation of the integral operator, the matrix A_{ij} is ill conditioned and has an infinite number of solutions. The proposed algorithm allows to narrow the class of possible solutions and to take into account *a priori* physical information about the solution:

1. The solution $\sum_j g_{ij}(r)$ must be such that when it is acted upon by the matrix of the integral operators A_{ij}, the residual norm should not exceed the error in the experimental data δ_i. This requirement is the main criterion to choose the approximate solution by the least-squares method.

$$\left\| \left(A_{ij}\, g_{ij} - u_i\right) \right\|_{L_2[c_i,d_i]} = \left\{ \int_{c_i}^{d_i} \sum_{j=1}^{n} \left| A_{ij}\, g_{ij} - u_i \right|^2 dk \right\}^{\frac{1}{2}} \quad \leq \quad \delta_i \tag{8}$$

   where c_i, d_i are the boundaries of experimental data set in k-space.

2. The solution $\sum_j g_{ij}(r)$ and its first derivative should be smooth.

3. The solution $\sum_j g_{ij}(r)$ should be positive at any r.

Let us single out three steps in the construction of regularisation algorithm.

Regularisation

As a regular approximate solution, we take the vector $\sum_j g_{ij}$, which minimises in space L_2 the Tikhonov functional:

$$\min M[g_{ij}] = \min\left\{ \left\| \sum_{j=1}^{n} (A_{ij} g_{ij} - u_i) \right\|^2 + \sum_{j=1}^{n} \left(\alpha_j \|g_{ij}\|^2 + \beta_j \left\| \frac{d}{dr} g_{ij} \right\|^2 \right) \right\}, \; g_{ij}(r) \in L_2[a_j, b_j] \tag{9}$$

The first term of Eq. (9) is the first physical requirement stated as Eq. (8). The presence of terms with small positive regularisation parameters α_j, β_j in the functional renders the problem stable and assures that the function $\sum_j g_{ij}$ and its first derivative are smooth.

Discrete approximation

To solve Eq. (9) numerically, the equation should be rewritten in discrete form. Approximating the space L_2 by the discrete space l_2 and prescribing in space l_2 the functions $g_{ij}(r)$, $u_i(k)$ as vectors and prescribing the integral operators $A_{ij}(k,r)$ as matrix, we receive the discrete analogue of Eq. (9). Using the fulfilment of the extremum condition (min M = 0), i.e. one finds a first variation derivative of the functional M with respect to the PCF g and sets it equal to zero, we obtain the system of linear algebraic equations:

$$\sum_{k=1}^{n} \left(A_{ij}^{*} A_{ik} + B_j \delta_{kj} \delta_{ij} \right) g_{jk} = A_{ij}^{*} u_i \qquad (j = 1,2,\ldots n) \tag{10}$$

Here B_j is the regularisation matrix:

$$B_j = \begin{vmatrix} \alpha_j + 2\beta_j & -\beta_j & 0 & \ldots & 0 \\ -\beta_j & \alpha_j + 2\beta_j & -\beta_j & \ldots & 0 \\ 0 & -\beta_j & \alpha_j + 2\beta_j & \ldots & 0 \\ \ldots & \ldots & \ldots & \ldots & \ldots \\ 0 & 0 & 0 & \ldots & \alpha_j + 2\beta_j \end{vmatrix} \tag{11}$$

In case of $UO_2(HAsO_4) \times 4H_2O$ compound for the U L3-edge let us rewrite Eq. (10): n = 3 and U, As, O correspond to 1,2,3, respectively, i.e. i = 1, j = 1,2,3.

$$\left\{\begin{vmatrix} A_{11}^{*}A_{11} & A_{11}^{*}A_{12} & A_{11}^{*}A_{13} \\ A_{12}^{*}A_{11} & A_{12}^{*}A_{12} & A_{12}^{*}A_{13} \\ A_{13}^{*}A_{11} & A_{13}^{*}A_{12} & A_{13}^{*}A_{13} \end{vmatrix} + \|B\|\right\} \times \begin{vmatrix} g_{11} \\ g_{12} \\ g_{13} \end{vmatrix} = \begin{vmatrix} A_{11}^{*}u_1 \\ A_{12}^{*}u_1 \\ A_{13}^{*}u_1 \end{vmatrix} \tag{12}$$

or in symbolic form:

$$(A^{*}A+B)g = A^{*}u \tag{13}$$

The eigenvalues of the regularised matrix ($A^*A + B$) are positive. In this case it is possible to use the well-known linear algebra methods to obtain a solution for Eq. (13). The inversion of the regularised matrix results in the so-called Tikhonov solution:

$$g_0 = (A^{*}A+B)^{-1}A^{*}u \tag{14}$$

Since the matrix ($A^*A + B$) is close to A^*A, it is obvious that for the exact Eq. (1) the Tikhonov solution is an approximate solution, which is stable and unique. It will serve as the starting solution for the following iteration procedure.

Iterational refinement

Let us consider the equation:

$$(A^{*}A+B)g_m = A^{*}u + Bg_m \tag{15}$$

which is equivalent to the exact Eq. (1). The number of the iteration is m. Assuming that the magnitudes of the elements of the regularisation matrix B are small compared with the elements of A, in a first approximation step the term Bg_m on the right side of Eq. (15) will be neglected. So, the Eq. (15) reduces to (13) with the known solution g_0.

The next steps to obtain more precise solutions g_m of Eq. (15) are:

$$g_m = (A^{*}A + B)^{-1}(A^{*}u + Bg_{m-1}) \qquad m = 1,2,\ldots, \tag{16}$$

In our case, we obtain the solutions g_m as a sum of peaks with lateral oscillations (see examples in Figures 3 and 4). During the iteration process we consider that two first peaks of the previous solution $g_{m-1}(r)$ can be described and replaced by the Gaussian functions. After substitution $g_{m-1}(r)$ in a new form to the right part of Eq. (16) we solve this equation and obtain a new solution $g_m(r)$. This assumption is valid if we know that our sample has a crystalline form. Thus, *a priori* physical information is introduced in the algorithm to obtain a reliable solution.

The iteration procedure is stopped when we compare the residual norm of each iteration solution $\|g_m\|$ with the previous one $\|g_{m-1}\|$ and obtain the minimum of this difference.

Here the norm of solution in discrete form g_m^p is:

$$\|g_m\| = \sqrt{\sum_p |g_m^p|^2} \tag{17}$$

The following main characteristics of the peak for the functions $g_{m-1}(r)$ have been selected: interatomic distances, the nearest neighbours co-ordination numbers and Debye-Waller (DW) factors. We estimated these values according to the Gauss functions describing the peaks of the solution.

Experimental

To be able to evaluate the results of our method, we chose a well-defined reference compound, $UO_2(HAsO_4) \times 4H_2O$ for the EXAFS analysis. The room temperature structure of this compound was determined by powder neutron diffraction using $UO_2(DAsO_4) \times 4D_2O$ [5]. Synthetic crystalline $UO_2(HAsO_4) \times 4H_2O$ was ground, mixed with an inert material and pressed into 13 mm diameter pellets. For the As K-edge and the U L3-edge measurements, the inert material was boron nitride and Teflon, respectively. The As K-edge and the U L3-edge EXAFS spectra were collected in transmission mode at sample temperatures of 41 K and 15 K, respectively, using a closed-cycle He cryostat. The measurements were performed at the Rossendorf Beamline (ROBL) at the European Synchrotron Radiation Facility (ESRF) using a Si(111) double-crystal monochromator in fixed-exit mode [6]. Harmonic suppression better than 8×10^{-4} was achieved by two Pt coated mirrors with a cut-off energy of 35 keV. In addition, the background absorption in the As K-edge spectrum was determined by measuring the absorption spectrum without any sample in the cryostat. For the U L3-edge spectrum, a Teflon pellet was used to measure the background absorption. The photon energy was calibrated using the L3-edge and K-edge energies of Au and Y foils at 11 919 eV and 17 038 eV, respectively.

The theoretical parameters, $f_j(k,r)$, $\delta_i(k)$, $\varphi_j(k,r)$ and $\lambda_i(k)$ were calculated with the software FEFF-8 [7] using the structural parameters of $UO_2(DAsO_4) \times 4D_2O$. For the U L3-edge the size of the cluster containing 717 atoms was 12.0 Å. For the As K edge the size of the cluster containing 699 atoms was 11.6 Å. The program FEFF-8 was also used to calculate the normalised oscillating parts $\chi_U(k)$ and$\chi_{As}(k)$ in single-scattering (SS) and multi-scattering (MS) approximations. For the MS calculation, all scattering paths with up to four legs were considered.

To compare the solution of the ill-posed problem, we calculated the partial PCFs, using the atomic co-ordinates obtained by ATOMS (subroutine of the FEFF-8 package) for the known structure of $UO_2(DAsO_4) \times 4D_2O$. The DW factor was arbitrarily set to $\sigma^2 = 0.003$ Å^2 for all elements.

For the transformation of the photon energy, E, into k, we used the following dispersion law: $E = ak^2 + bk + c$. The parameters a, b and c were determined by a least-square fit of the energy of several extrema in the EXAFS region of the experimental spectrum in E space to the corresponding k values of the theoretical $\chi_i(k)$. For the U L3-edge (As K edge) the obtained parameters are a = 3.82 (3.66), b = -0.16 (2.90), and c = 17 179 (11 856). This procedure ensures that the ionisation potential for the experimental $\chi_i(k)$ is the same as that calculated by FEFF-8.

Results and discussion

Figure 1 compares the theoretical normalised oscillating $\chi_U(k)$ calculated in SS approximation with that obtained in MS approximation. Although the two curves show some differences at low k values, the contribution of MS effects is rather small and should be negligible at least for the first uranium neighbours. As can be seen from Figure 2, the theoretical $\chi_U(k)$ in MS approximation reproduces the main features of the experimental data well. This confirms the correctness of our conversion from photon energy into k space. Small deviations between the two spectra are mainly due to differences in the DW factors.

The partial PCFs for the pairs U-U, U-As and U-O were obtained from the experimental $\chi_U(k)$ and are compared to the corresponding model functions in Figure 3. As one can see, the positions of the first two peaks of each pair agree well with the expected positions. However, there is a distinct shift for the U-U_2 peak in r space toward larger values. The differences in peak heights are due to the assumed DW factors for the model function.

The comparison of the experimental and the model partial PCFs As-U, As-As and As-O are given in Figure 4. Except for the second shell of the As-As pair, the experimental peak positions coincide with those of the model functions. The As-As_2 peak has a lower r-value than the true position.

For the known crystal structure, it is possible to calculate the MS contributions and eliminate them from the experimental data. By subtracting the MS contribution shown in Figure 1 from the experimental data shown in Figure 2, we obtained new "experimental" data that should contain only SS contributions. In Tables 1-3, we refer to the modified (original) experimental data as Tikhonov SS method (Tikhonov MS method). As one can see from the interatomic distances given in Table 1, after correction for MS effects we obtain good agreement with neutron data [7] not only for the first shell but also for all second shells in all partial PCFs. The co-ordination numbers and DW factors given in Tables 2 and 3 were obtained by fitting a Gaussian line shape to the peaks of the first shell in the partial PCFs. The co-ordination numbers agree well with the expected values. For the U-O PCFs, the co-ordination number of the second shell is also in good agreement with the crystal structure. For the shells U-As and As-U the obtained structural parameters agree with each other and are independent from the central atom (see Tables 1-3).

In conclusion, a new special iterative algorithm was proposed to solve the integral EXAFS Eq. (1), which is an inverse, ill-posed problem. The procedure was applied to the analysis of As K-edge and U L3-edge EXAFS spectra of the ternary system $UO_2(HAsO_4) \times 4H_2O$, for which the crystal structure is known. Three partial PCFs could be determined for each EXAFS spectrum. For the first shells, the interatomic distances and co-ordination numbers agree with the expected values. However, MS effects can cause peaks of the second shell to be shifted relative to the true value. The main advantage of this method compared to other methods for EXAFS analysis is that the presence of a certain co-ordination shell and its interatomic distance can be detected without any structural model. This method has great potential, especially for the EXAFS analysis of systems with closely spaced co-ordination shells of the same or different type of atoms.

Acknowledgements

We thank M. Rutsch for the synthesis of $UO_2(HAsO_4) \times 4H_2O$ and C. Hennig and A. Rossberg for their assistance during the EXAFS measurements at BM20 at the ESRF.

REFERENCES

[1] D.E. Sayers, E.A. Stern, F.W. Lytle, *Phys.Rev.Lett.*, 27, 1204 (1971).

[2] A.N. Tikhonov, V.Ya. Arsenin, “Solution of Ill-posed Problems”, John Wiley and Sons, Inc., New York (1981).

[3] Yu.A. Babanov, V.V. Vasin, A.L. Ageev, N.V. Ershov, *Phys. Stat. Sol. (b)*, 105, 747 (1981).

[4] N.V. Ershov, A.L. Ageev, V.V. Vasin, Yu.A. Babanov, *Phys. Stat. Sol. (b)*, 108, 103 (1981).

[5] A.N. Fitch, L. Bernard, A.T. Howe, A.F. Wright, B.E.F. Fender, *Acta Cryst.*, C39, 159 (1983).

[6] W. Matz, N. Schell, G. Bernhard, F. Prokert, T. Reich, J. Claussner, W. Oehme, R. Schlenk, S. Dienel, H. Funke, F. Eichhorn, M. Betzl, D. Proehl, U. Strauch, G. Huttig, H. Krug, W. Neumann, V. Brendler, P. Reichel, M.A. Denecke, H. Nitsche, *J. Synchrotron Rad.*, 6, 1067 (1999).

[7] A.L. Ankudinov, B. Ravel, J.J. Rehr, S.D. Condradson, *Phys. Rev. B*, 58, 7565 (1998).

Figure 1. Theoretical U L3-edge $\chi(k)$ of $UO_2(HAsO_4) \times 4H_2O$ calculated in single -scattering (SS) approximation (solid line) and multi-scattering (MS) approximation (dashed line). The difference between MS and SS approximations is shown as dotted line.

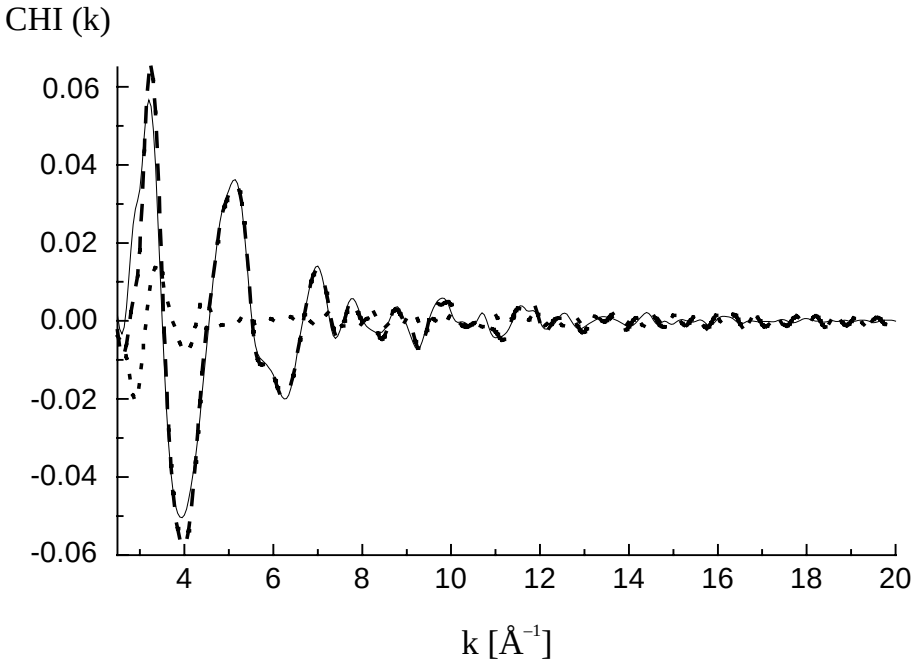

Figure 2. Experimental (solid line) and theoretical U L3-edge $\chi(k)$ (dashed line) of $UO_2(HAsO_4) \times 4H_2O$. The theoretical $\chi(k)$ was calculated in MS approximation.

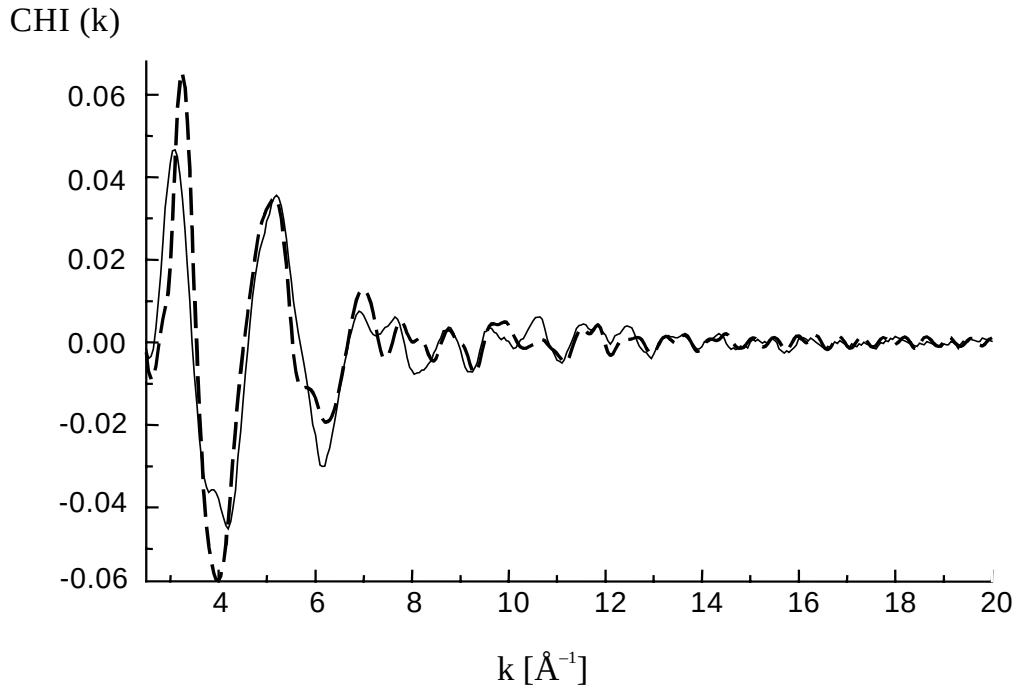

Figure 3. Comparison of experimental partial pair correlation functions (dashed line) and corresponding model functions (solid line) for $UO_2(HAsO_4) \times 4H_2O$. The experimental curve was obtained from U L3-edge $\chi(k)$.

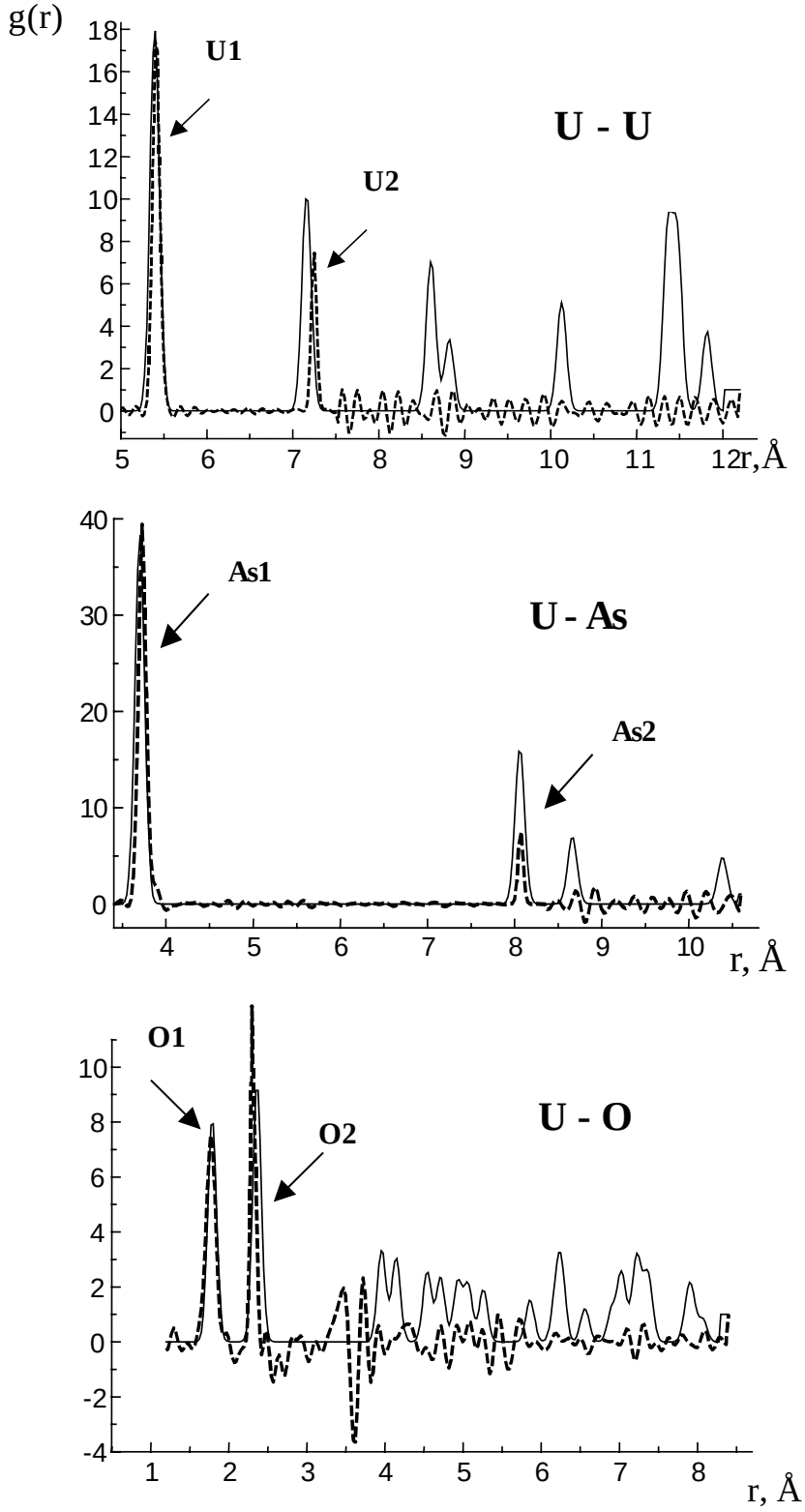

Figure 4. Comparison of experimental partial pair correlation functions (dashed line) and corresponding model functions (solid line) for $UO_2(HAsO_4) \times 4H_2O$. The experimental curve was obtained from As K-edge $\chi(k)$.

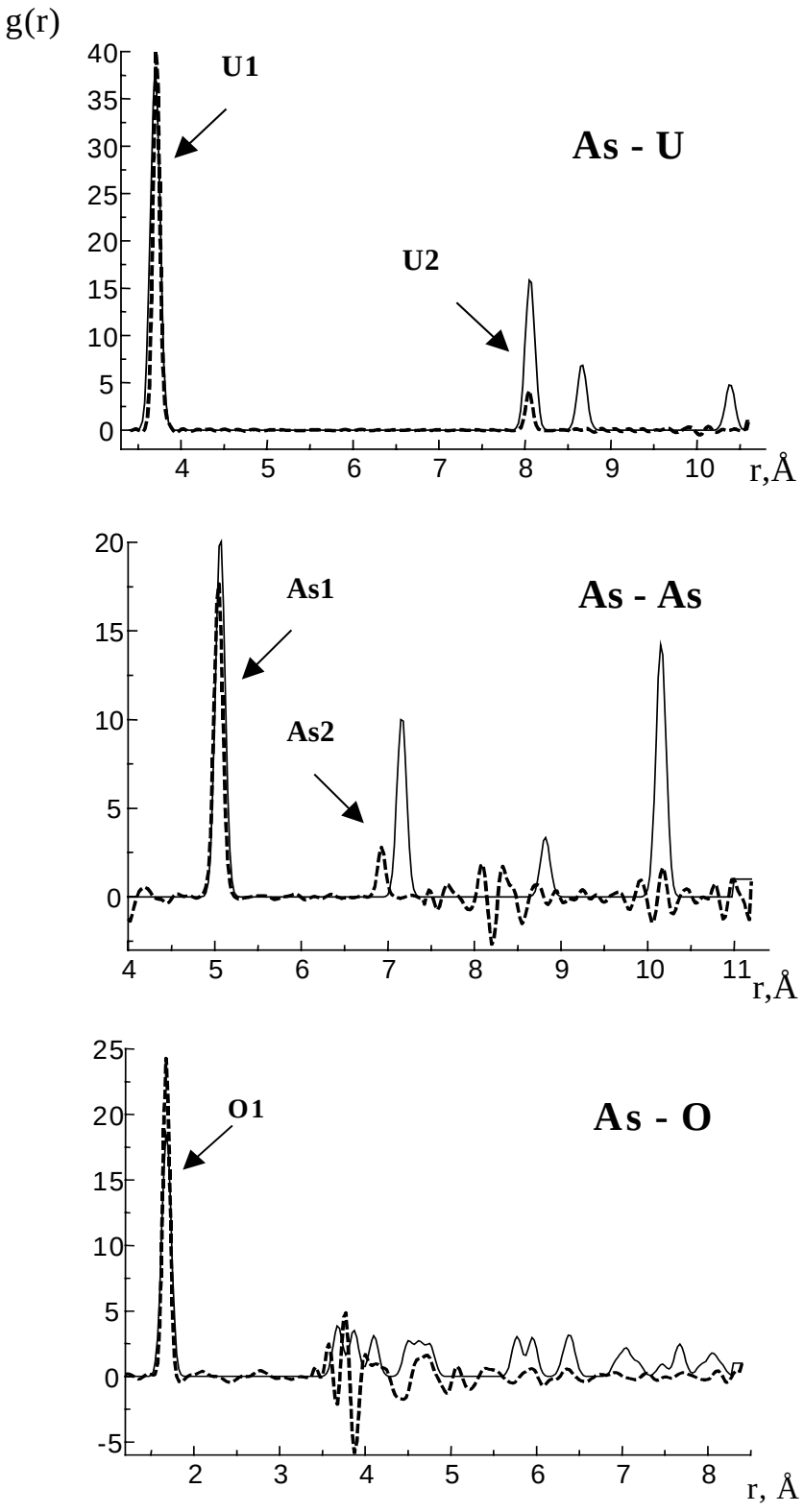

Table 1. Interatomic distances in Å for $UO_2(HAsO_4) \times 4H_2O$ (15 K)

Shell	Tikhonov SS method	Tikhonov MS method	Neutron diffraction
$U\text{-}U_1$	5.42	5.42	5.39
$U\text{-}U_2$	7.16	7.01	7.16
$U\text{-}As_1$	3.73	3.73	3.70
$U\text{-}As_2$	8.08	8.07	8.06
$U\text{-}O_1$	1.77	1.78	1.78-1.79
$U\text{-}O_2$	2.33	2.32	2.30
$As\text{-}U_1$	3.68	3.71	3.70
$As\text{-}U_2$	8.06	8.04	8.06
$As\text{-}As_1$	5.07	5.04	5.06
$As\text{-}As_2$	7.17	6.94	7.16
$As\text{-}O_1$	1.68	1.68	1.68
$As\text{-}O_2$	3.76	3.77	3.68-3.88

Table 2. Co-ordination numbers for $UO_2(HAsO_4) \times 4H_2O$ (15 K)

Shell	Tikhonov SS method	Tikhonov MS method	Neutron diffraction
$U\text{-}U_1$	4.2	4.3	4.0
$U\text{-}As_1$	4.0	3.8	4.0
$U\text{-}O_1$	2.1	2.0	2.0
$U\text{-}O_2$	4.0	3.8	4.0
$As\text{-}U_1$	4.0	3.9	4.0
$As\text{-}As_1$	4.3	4.1	4.0
$As\text{-}O_1$	3.8	3.9	4.0

Table 2. Debye-Waller factors in $Å^2$ for $UO_2(HAsO_4) \times 4H_2O$ (15 K)

Shell	Tikhonov SS method	Tikhonov MS method
$U\text{-}U_1$	0.003	0.004
$U\text{-}As_1$	0.002	0.002
$U\text{-}O_1$	0.004	0.004
$U\text{-}O_2$	0.002	0.002
$As\text{-}U_1$	0.001	0.002
$As\text{-}As_1$	0.002	0.004
$As\text{-}O_1$	0.002	0.002

EVOLUTION OF THE ELECTRONIC AND STRUCTURAL PROPERTIES OF $AnFe(CN)_6 \cdot xH_2O$ (An = Th, U, Np, Pu, Am) COMPOUNDS: AN X-RAY ABSORPTION SPECTROSCOPY STUDY

Isabelle Bonhoure,[1,6] **Christophe Den Auwer,**[1,6] **Christophe Cartier dit Moulin,**[2,6] **Philippe Moisy,**[1] **Jean-Claude Berthet,**[3] **S. Conradson**[5] **and Charles Madic**[4]

[1]CEA Marcoule, DCC/DRRV/SEMP, F-30207 Bagnols-sur-Cèze, France

[2]Laboratoire de Chimie Inorganique et Matériaux Moléculaires, ESA CNRS 7071, Université Pierre et Marie Curie, 4, Place Jussieu, F-75252 Paris Cedex 05, France

[3]CEA Saclay, DSM/DRECAM/SCM, F-91190 Gif-sur-Yvette, France

[4]CEA Saclay, DCC, F-91190 Gif-sur-Yvette, France

[5]Los Alamos National Laboratory

[6]LURE, Centre Universitaire Paris-Sud, Bât. 209 D, BP 34, F-91898 Orsay Cedex, France

Abstract

It is well known that new three-dimensional molecular structures can be obtained through the use of well-characterised building blocks. Such methods have been widely used to obtain pre-organised three-dimensional entities. Among possible building blocks, the hexacyano metallate ions $[M(CN)_6]^{n-}$ are often used to form polymeric inorganic networks such as Prussian Blue $Fe_4[Fe(CN)_6]_3 \cdot 15H_2O$. Recently, the possibility to form $An[M(CN)_6]$ solids has been evidenced [1].

The structural study of $An[M(CN)_6]$ complexes is of great interest, all the more because of their possible applications in nuclear fuel reprocessing. As microcrystalline materials were obtained, X-ray powder diffraction (XPD), infrared (IR) and X-ray absorption (XAS) spectroscopies were of particular help to probe the An and Fe environments. We investigated the long-range order using XRPD. The IR vibration bands of the cyano groups probe the chemical bonds of the carbon and nitrogen atoms in these new materials. XAS provides both information about the electronic structure via X-ray absorption near edge spectroscopy (XANES) and about the local structure around the metals via extended X-ray absorption fine structures spectroscopy (EXAFS). Moreover, the evolution of the properties of these new complexes along the actinide series is an indirect probe of the actinide bonding [2].

REFERENCES

[1] a. Y.M. Kulyako, T.I. Trofimov, D.A. Malikov, I.A. Lebedev and B.F. Myasoedov. *Radiochem.*, 35(4), 399 (1993).

b. Y.M. Kulyako, T.I. Trofimov, D.A. Malikov, I.A. Lebedev and B.F. Myasoedov. *Radiochem.*, 35(5), 549 (1993).

c. Y.M. Kulyako, D.A. Malikov, T.I. Trofimov and B.F. Myasoedov, *Mendeleev Commun.*, 173 (1996).

[2] I. Bonhoure, C. Den Auwer, C. Cartier dit Moulin, P. Moisy, J-C. Berthet and C. Madic, accepted for publication in *Can. J. Chem.* CHEM 00-006-OR.

SR-BASED X-RAY MICROBEAM TECHNIQUES UTILISED FOR SOLID-STATE SPECIATION OF U IN FUEL PARTICLES

B. Salbu,[1] **K. Janssens,**[2] **O.C. Lind,**[1] **A. Simionovici,**[3]
T. Krekling,[1] **M. Drakopoulos,**[3] **I. Snigireva,**[3] **A. Snigirev**[3]
[1]Department of Chemistry and Biotechnology, Agricultural University of Norway, Aas, Norway
[2]Department of Chemistry, University of Antwerp, Antwerp, Belgium
[3]European Synchrotron Radiation Facility, Grenoble, France

Abstract

To assess the impact of radioactive particle contamination of different ecosystems, information on particle characteristics such as structure and oxidation states of matrix elements influencing weathering and mobilisation of associated radionuclides is essential. In the present work, gamma measurements have been combined with different solid-state speciation techniques, i.e. scanning electron microscopy (SEM) and different synchrotron radiation (SR) based X-ray microbeam techniques to characterise the structures and oxidation states of uranium in fuel (UO_2) particles released from the Chernobyl reactor [1]. During the initial explosion mechanical destruction of fuel occurred and released fuel particles were characterised as inert U, probably reduced U, with low weathering rates. Particles released during the subsequent reactor core fire contained oxidised U and the weathering rates were high. Thus, SR based μ-XAS tomography and μ-XANES proved to be highly useful techniques for characterising radioactive particles and the results obtained are essential for the impact assessments of particle-associated radionuclides.

Introduction

Following nuclear events such as nuclear weapons tests, nuclear accidents and effluent discharges from nuclear installations, a major fraction of refractory radionuclides released to the environment is associated with radioactive particles [2-7]. With time, particle weathering occurs and mobilised radionuclides are subjected to biological uptake and ecosystem transfer. Information on source-dependent and release-related particle characteristics and weathering rates is therefore essential to assess long-term impacts for areas contaminated by radioactive particles. During the Chernobyl accident about 6-8 tonnes of uranium fuel were released [2] and fuel particles were identified up to 2 000 km from the site (e.g. Norway). During the initial explosion mechanical destruction of fuel occurred and fuel particles were deposited to the west of the reactor. During the subsequent reactor core fire, however, fuel particles deposited to the north. Thus, the particles deposited after the Chernobyl accident originated from the same reactor core, but were released under different temperature, pressure and oxic/anoxic conditions which should be expected to influence the structure and oxidation states.

Experimental methods and instrumentation

Sample preparation

Radioactive particles were separated from soil and dust samples collected to the west and north of the Chernobyl reactor in the period 1990-1994. The isolation of individual particles from soil and dust samples is a tedious time-consuming task and the work includes:

- Autoradiography and γ-spectrometry to identify hot spots.
- Isolation of individual particles using light microscopy.
- Mounting of individual particles on stubs, tape or capillary.
- Screening with scanning electron microscopy (SEM) interfaced with an X-ray microanalyser (XRMA).

Using SEM with XRMA, the information obtained on surface structures and elemental distributions in individual particles techniques [8] is essential for further detailed studies using SR-based X-ray microbeam. Furthermore, XRF screening of particles using a second-generation synchrotron radiation source (e.g. HASYLAB, Germany) has proven useful, as subsurface hot spot areas of elements of interest can be identified prior to the application of X-ray microbeam techniques (i.e. μ-XAS tomography, μ-XRD and μ-XANES).

Micro-tomography and micro-imaging

To obtain information on the 3-D distribution of elements in individual particles, μ-XAS tomography was performed at ESRF, beamline ID22**.** Each individual particle was mounted on a glass capillary (Figure 1), which was placed on a micro-tomography stage with 8 degrees of freedom for alignment and rotation. The sample was rotated around a horizontal axis to obtain the highest resolution in the plane of reconstruction. During rotation, images were recorded at 17 keV with a high resolution, cooled CCD-based X-ray detector with a resolution of 0.6 μm [9]. Monochromator tuning allows also the formation of images as a function of incident photon energy to perform XANES imaging (2-D oxidation state mapping) and X-ray absorption near-edge tomography (XANET) [9].

Figure 1. Particle glued on glass capillary

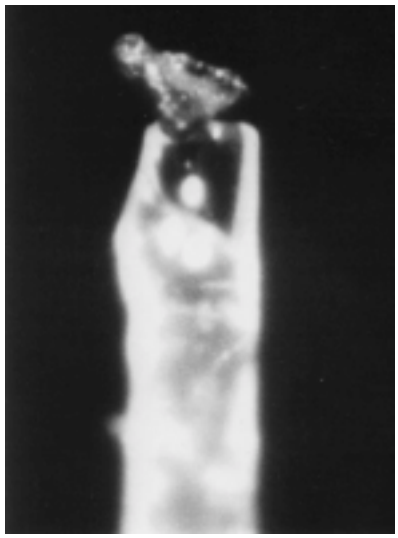

μ-XAS, μ-XRF, μ-XRD and μ-XANES

To obtain information on the composition, crystallographic structure and oxidation states of elements contained in a particle on a submicrometer scale, μ-XAS, μ-XRF, μ-XRD and μ-XANES were combined using hard X-ray microbeams at ID22. X-ray radiation from the undulator (source size 35 μm vertically and 700 μm horizontally) passed through a Si monochromator providing an X-ray beam at selected fundamental energy. The fixed exit double crystal monochromator allowed tuning of the energy over absorption edges, while keeping the beam position on the sample. The monochromatic X-ray beam was focused by a Fresnel Zone Plate to a spot of about 1.5 μm vertically and 5 μm horizontally on a sample at 0.7 m distance. The absolute flux at the beamspot on the sample was 10^9 photons/s at 17 keV. U-particles mounted on carbon tape or on capillaries were placed on the sample stage having three translations and one rotation axis. Long working distance optical microscope and a high resolution X-ray CCD camera were used to position the sample in the focused X-ray beam. To calibrate the results obtained, standards well-defined with respect to crystallographic structures and oxidation states were applied (U_{met}, UO_2, U_3O_8 and $UO_2Ac_2{\cdot}2H_2O$). The absorption spectra (μ XAS, μ XANES) were recorded with pindiodes, while the fluorescence (μ-XRF) spectra were recorded using a Si(Li) energy dispersive detector having an area of 12 mm^2 mounted at 90º to the incident beam and 15 mm from the samples.

In micro-diffraction (μ-XRD) the particles and standards were exposed for 3-10 minutes at different energies between 17 keV and 25 keV. Debye-Scherrer rings were recorded at 200 mm distance from the sample using a Fujitsu image plate (A4 format, resolution of 100×100 μm). The plate was optically scanned with a Molecular Dynamics scanner and processed to yield information on the diameter of the Debye-Scherrer rings. The penetration depth in particles was about 50 μm. Micro-diffraction (μ-XRD) allowed local crystallographic structures to be determined, demonstrating that UO_2 fuel was transformed during the release scenarios.

The μ-XANES spectra of particles and standards were obtained by scanning the X-ray energy over the U L_{III} absorption edge, while measuring the incident and transmitted beam intensity (I_0, I) with pindiodes. By determining the inflection point energy as a function of photon energy for the

standards, a correlation between the inflection point energy and oxidation state was obtained [1]. By performing a μ-XANES line scan, i.e. positioning the X-ray microbeam at various locations along a line through the particle and determining the first inflection point of the local XANES profile, the distribution of the U oxidation state across the particles was attained. The distribution of oxidation states of U within the particles was determined from a series of absorption images covering the particle. In each pixel the oxidation state was determined from the location of the first inflection point.

Results and discussion

Using μ-XAS tomography, information on the 3-D distribution of U in a fuel particle released during fire in the Chernobyl reactor [Figure 2(a)] was obtained. In addition, tomographic reconstruction and computerised slicing of the 3-D image [Figure 2(b)] demonstrated that U was inhomogeneously distributed within the particles. The porosity of the particles was attributed partly to channels and cavities produced during reactor operation by the formation of volatile radionuclides and partly to the fact that U had been oxidised during the release.

Figure 2

(a) μ-XAS tomography of an oxidised fuel particle released during the fire in the Chernobyl reactor.

(b) Computerised slicing of the 3-D image of the oxidised fuel particle.

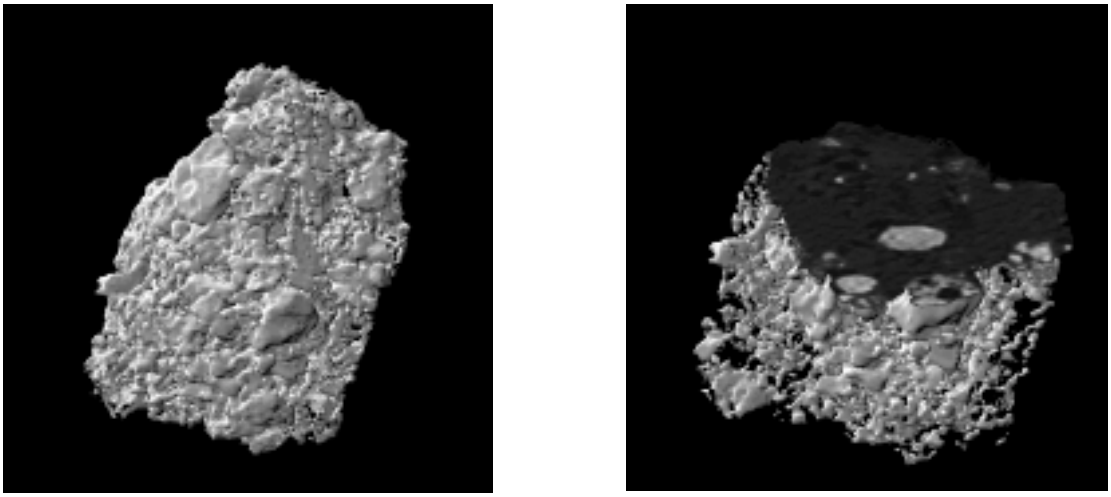

The μ-XRD results demonstrated that U in the UO_2 fuel particles released during the reactor fire (north of the reactor) was oxidised to U_3O_8 and U_2O_5. These findings were further supported by the μ-XANES images, showing a shift in the inflection point energy corresponding to that of the oxidised standards. The 2-D μ-XANES imaging (Figure 3) also demonstrated that the particles released during the fire were characterised by UO_2 cores surrounded by oxidised U (U_2O_5/U_3O_8 layers).

In contrast, the μ-XRD results demonstrated that U in crystalline fuel particles released during the explosion (west of the reactor) probably was reduced, as no sign UO_2 and oxidised forms could be observed. These findings were also supported by the μ-XANES images, showing a shift in the inflection point energy corresponding to oxidation states lower than 4 (UO_2). Thus, the different release conditions influenced the characteristics of fuel particles, originally present as UO_2, emitted from the reactor core.

Figure 3. μ-XANES imaging of a particle collected to the north of the Chernobyl reactor, released during the reactor fire. The particle has a UO_2 core surrounded by an oxidised U_2O_5/U_3O_8 surface layers.

Conclusions

Particle characteristics such as crystallographic structures and oxidation states influence the weathering and mobilisation of radionuclides associated with radioactive particles. As demonstrated in the present work, the crystallographic structures and oxidation states of uranium in fuel particles released from the Chernobyl reactor depended on the release conditions. Particles released during the initial explosion under high-temperature and high-pressure conditions contained reduced U, while particles released during the subsequent fire, lower temperature and aerobic conditions contained oxidised U. Thus, differences in crystallographic structures and oxidation states of uranium in fuel particles explain the observed differences in weathering kinetics, mobility and soil-to-vegetation transfer coefficients of radionuclides associated with particles located west and north of the Chernobyl reactor [10]. The present work also demonstrated that the combination of SR-based X-ray microscopic techniques provides essential solid-state speciation information, i.e. spatial elemental distributions, crystallographic structures and oxidation states influencing the weathering and mobilisation of particle-associated radionuclides, of importance for impact assessments of particle contaminated ecosystems and should be utilised within radioecology.

REFERENCES

[1] B. Salbu, K. Janssens, T. Krekling, A. Simionovici, M. Drakopoulos, C. Raven, I. Snigireva, A. Snigirev, O.C. Lind, D.H. Oughton, F. Adams and V.A. Kashparov, "μ-XAS Tomography and μ-XANES for Characterisation of Fuel Particles", ESRF Highlights 1999, European Synchrotron Research Facility, Grenoble, France (2000).

[2] N.V. Victorova and E.K. Garger, "Biological Monitoring of the Deposition and Transport of Radioactive Aerosol Particles in the Chernobyl NEP Zone of Influence", Proc. CEC seminar on Comparative Assessment of the Environmental Impact of Radionuclides Released During Three Major Nuclear Accidents", Kyshtym, Windscale, Chernobyl, EUR 13574, 223-236 (1990).

[3] M. Cooper, P. Burns, B. Tracy, M. Wilks and G. Williams, "Characterisation of Plutonium Contamination at the Former Nuclear Weapons Testing Range at Maralinga in South Australia", *J. Radioanal. Nucl. Chem*., 177, 161-184 (1994).

[4] P.R. Danesi, *et al*., Proceedings of the 7th Int. Conf. on Low-level Measurements of Actinides and Long-lived Radionuclides in Biological and Environmental Samples, University of Utah, Salt Lake City, September 1998.

[5] L. Devell, M. Tovedal, U. Bergström, A. Applegren, J. Chussler and L. Andersson, "Initial Observations of Fallout from the Reactor Accident of Chernobyl", *Nature*, 321, 817 (1986).

[6] B. Salbu, T. Krekling, D.H. Oughton, G. Östby, V.A. Kashparov, T.L. Brand and J.P. Day, "Hot Particles in Accidental Releases from Chernobyl and Windscale Nuclear Installations", *Analyst*, 119, 125-130 (1994).

[7] B. Salbu, "Actinides Associated with Particles", *J. Environ. Radioact. Booklets*, in press.

[8] B. Salbu, T. Krekling and D.H. Oughton, "Characterisation of Radioactive Particles in the Environment', *Analyst*., 123, p. 843-849 (1998).

[9] A. Koch, C. Raven, P. Spanne and A. Snigirev, "X-ray Imaging with Submicrometer Resolution Employing Transparent Luminescent Screens", *J. Opt. Soc. Am. (A)*, 15, 1940-1951 (1998).

[10] V.A. Kashparov, D.H. Oughton, V.P. Protsak, S.I. Zvarisch and S.E. Levchuk, "Kinetics of Fuel Particle Weathering and ^{90}Sr Mobility in the Chernobyl 30 km Exclusion Zone", *Health Physics*, 76, 251-259 (1999).

SYNCHROTRON X-RAY MICROPROBE: COMBINED TECHNIQUES FOR THE ANALYSIS OF ENVIRONMENTAL PARTICLES

M. Drakopoulos
ESRF, France

Abstract

The high brightness of synchrotron radiation sources of the third generation and the development of optical elements for X-rays make it possible to create micro-beams of micrometer size and smaller with high intensity. These beams can be used to reveal spatially resolved information about structural and chemical properties of particles. The accessible energy range of above 10 keV allows to excite fluorescence of most elements and as well to obtain crystallographic information.

In fluorescence mode very low concentrations of less then 0.1 ppm can be routinely detected. The trace elements analysis on micro-particles makes possible to follow environmental problems with very high sensitivity and without destructive sample treatment. The local resolution allows tracking the interplay between the active component and the host matrix.

Via micro-diffraction we access structural information, which may answer questions about the chemical state, about links between the matrix structure and the absorbed components and about the mineralogical phases the particles consist of. Both methods are complementary and can be performed simultaneously. In combination with micro-imaging methods such as micro-tomography we can obtain a good understanding about the properties of micro-particles.

SIMS AND NUCLEAR TRACK METHODS FOR THE CHARACTERISATION OF ACTINIDE-CONTAINING PARTICLES IN ENVIRONMENTAL SAMPLES

M. Betti, N. Erdmann, G. Tamborini, P. Carbol
European Commission, Joint Research Centre, Institute for Transuranium Elements
P.O. Box 2340, 76125 Karlsruhe, Germany

Abstract

The effectiveness of alpha and fission nuclear track analyses for the localisation of particles containing actinides in samples from different origins is discussed. Information from the latter is combined with results from secondary ion mass spectrometry (SIMS) and scanning electron microscopy (SEM) to obtain chemical and isotopic characterisation, as well as to determine the samples' morphologies.

Introduction

A variety of systems and processes may introduce radioactivity in the environment. Human activities involving nuclear weapons and nuclear fuel cycle can lead to a significant formation and potential release of radioactivity. Technology may also release pre-existing natural radionuclides which would otherwise remain trapped in the earth's crust. A general distinction can be made between gases, aerosol and particulate materials.

Particles exhibiting a very high activity are usually called "hot particles" or "radioactive particles". They may be produced in atmospheric nuclear weapon tests or nuclear reactor accidents and can be formed by two processes: disintegration of the nuclear fuel mass or condensation of evaporated products. These radioactive particles can be transferred to soil and water directly or via vegetation and movement through other biota.

The chemical and isotopic characterisations of these particles, as well as their morphological structure, are of fundamental importance for determining their diffusion mechanisms. In this presentation the methods based on nuclear tracks combined with SIMS and SEM measurements for the characterisation of these particles are discussed.

Nuclear track methods

In order to facilitate the localisation of the interesting particles, screening techniques are used. In our laboratory the use of nuclear track detection techniques for the localisation of actinide-containing particles in swipe and soil samples has been exploited. Procedures for α autoradiography and fission track detection have been developed and applied to various environmental samples of different origins. An example of α tracks created from hot spots in the analysis of a humus layer from the Chernobyl region is shown in Figure 1. It can be seen that several particles can be identified. As for their chemical and isotopic characterisation they must be measured by other techniques. The first test is performed by SEM/EDX for the chemical composition of the particles then their isotopic composition is measured by SIMS. Assuming a detection probability of α particles in the film of 100% [1] and a geometric detection efficiency of 40%, the total α activity in these spots, containing *c.a.* 600 tracks yields 0.48 mBq. From this result and those from SEM/EDX and SIMS these α spots could stem from a small fragment of Chernobyl reactor fuel. The α activity is due to low-enriched uranium as well as plutonium and americium.

The fission track method has been exploited mainly for the screening of samples after recovering of particles from swipe samples. In Figure 2 the image of the tracks obtained for one particle is illustrated.

The same particle was investigated by SEM analysis using the back-scattered mode of the microscope. The EDX spectrum showed clearly that the particle consisted of uranium. Further, by SIMS it was possible to measure the isotopic composition of this particle and correlate that with its size and number of fission tracks developed, by the use of standard particles obtained from reference materials with well-known isotopic composition [4].

In Figure 3 the SEM image (a) and the EDX spectrum (b) are shown. Figure 4 gives the image obtained by SIMS. As can be seen, both techniques can provide information relevant to the particle dimension.

Figure 1. α tracks of a hot spot from the analysis of the humus layer. The exposure time was 46 days. The total number of α tracks is approximately 600, which corresponds to an activity level of ≈ 0.5 mBq.

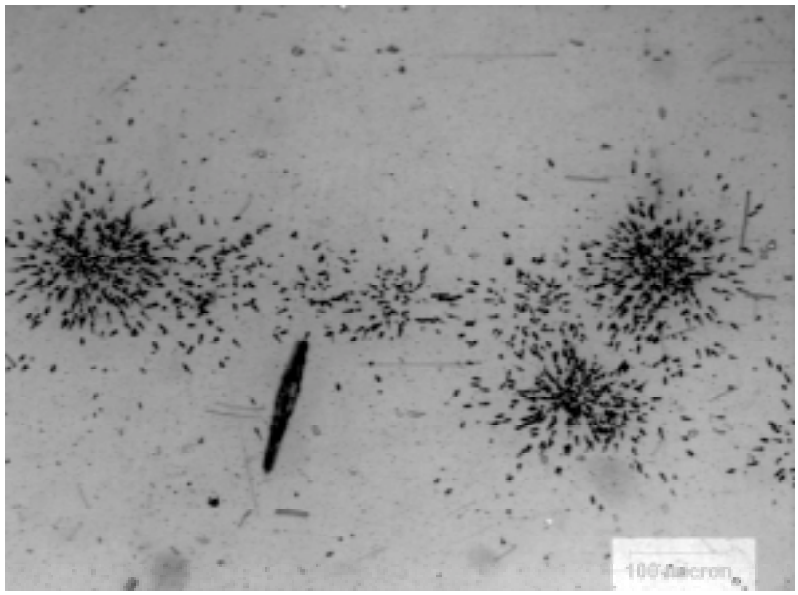

Figure 2. Fission track image of a particle from a swipe sample

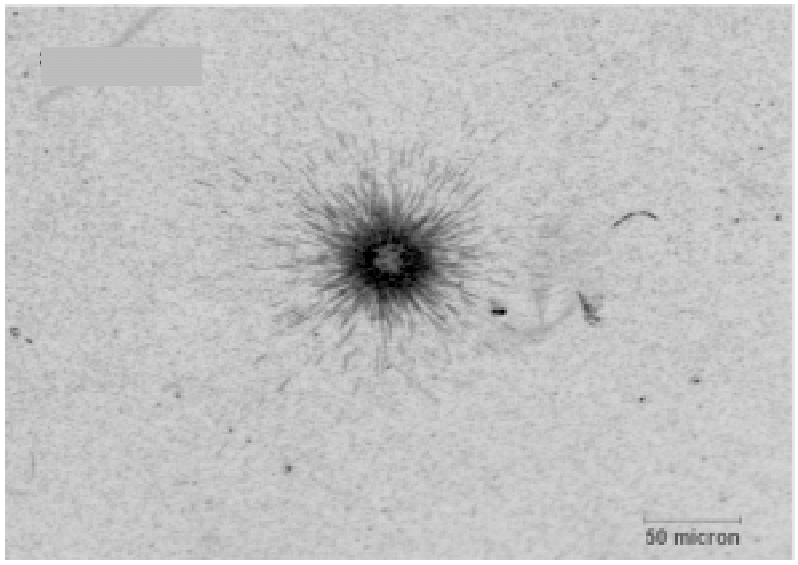

Figure 3. (a) SEM image of a uranium-containing particle from a swipe sample, located by FT analysis (see Figure 2). (b) EDX spectrum of the particle shown in (a).

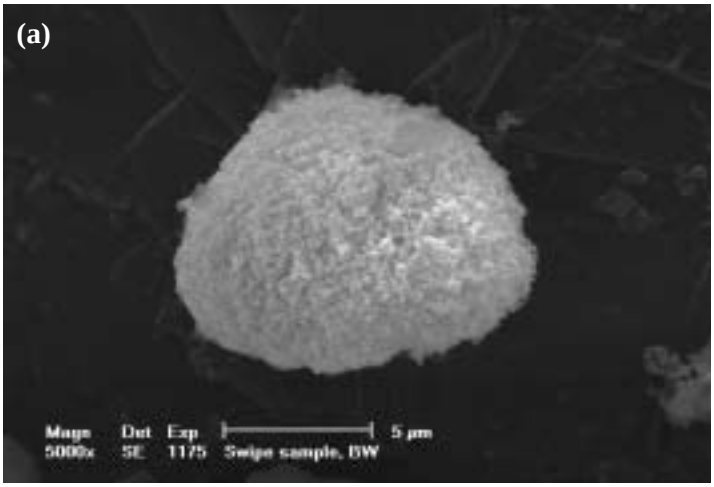

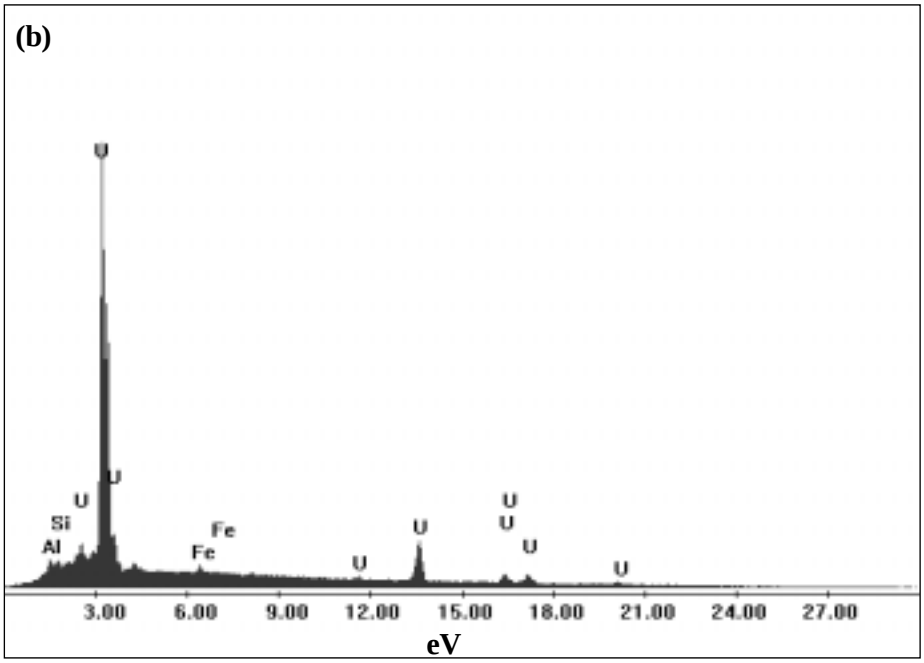

Figure 4. Secondary ion image of a uranium particle from a swipe sample, located by fission track detection and analysed by SEM and SIMS

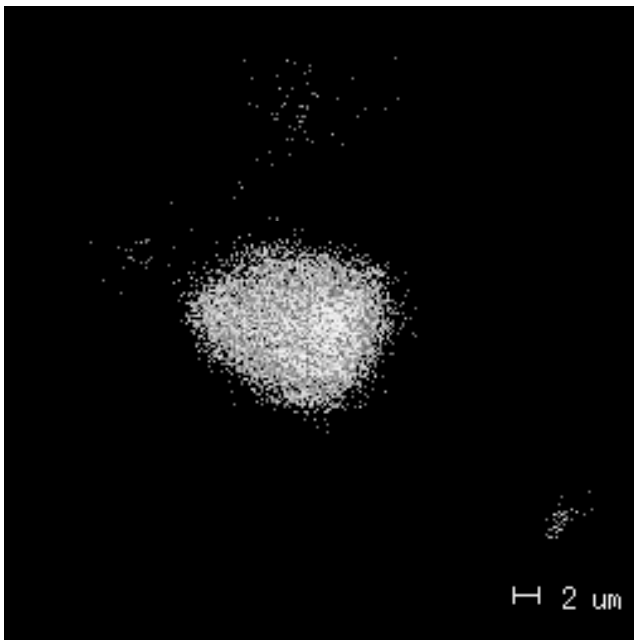

SIMS applications

Secondary ion mass spectrometry is used to verify the isotopic composition of particles [2,3] and their chemical composition. A typical application has been demonstrated on control particles consisting of uranium oxide produced in our laboratory [4].

Four batches of uranium oxide particles of 1 μm size having a different enrichment in ^{235}U were obtained. In Table 1 [4] the results obtained by SIMS for the isotopic characterisation of the produced particles are reported. It can be seen that for the measurement of the ratio $^{235}U/^{238}U$ an accuracy of better than 0.5% was obtained with a typical precision of 1%. As for the minor isotopes (^{234}U and ^{236}U with respect to ^{238}U), an accuracy of a few per cent was achieved.

The technique has also been exploited for the characterisation of plutonium particles. In Figure 5 the SIMS images obtained for the two different Pu particles are shown [5].

From the SIMS measurements the dimensions of the particles can also be obtained and compared with those from SEM. Clearly, only SEM can provide the particle structure. On the other hand, SIMS provides the unique information on the isotopic composition of the particles.

Conclusions

The combination of nuclear track methods with SIMS allows different radioactive and actinide-containing particles to be localised and to be characterised as for their chemical content and isotopic composition. SEM is used to obtain complementary information on the morphology of particles.

Further research with other techniques in order to obtain information on the speciation is ongoing.

Table 1. SIMS isotopic ratios obtained for uranium oxide particles from four different certified standard reference uranium materials: CRM U005, U010, U030 and U100

The certified and measured values for the 234/238, 235/238 and 236/238 U ratios together with % bias and % rsd are given. The 236/238 U ratio was corrected for the contribution of $^{235}UH^{+}$ using the signal on mass 239 ($^{238}UH^{+}$), except for U005.

		U005	U010	U030	U100
$^{234}U/^{238}U$	Certified value	2.19 E-5	5.46 E-5	1.96 E-4	7.54 E-4
	Measured value	(2.62 ± 0.95) E-5	(5.85 ± 0.57) E-5	(1.96 ± 0.07) E-4	(7.54 ± 0.12) E-4
	Precision (rsd%)	36.4	9.7	3.8	1.5
	Accuracy (bias%)	19.41	6.92	-0.23	0.13
$^{235}U/^{238}U$	Certified value	4.92 E-3	1.01 E-2	3.15 E-2	1.14 E-1
	Measured value	(4.90 ± 0.05) E-3	(1.02 ± 0.01) E-2	(3.15 ± 0.01) E-2	(1.14 ± 0.01) E-1
	Precision (rsd%)	1.1	1.0	0.3	0.8
	Accuracy (bias%)	-0.39	0.15	0.13	0.06
$^{236}U/^{238}U$	Certified value	4.68 E-5	6.87 E-5	2.10 E-4	4.23 E-4
	Measured value	(4.34 ± 0.32) E-5	(6.49 ± 0.51) E-5	(2.17 ± 0.20) E-4	(4.25 ± 0.27) E-4
	Precision (rsd%)	22.0	7.9	9.1	6.2
	Accuracy (bias%)	-7.3	-5.53	3.09	0.62

Figure 5. SIMS images for ^{239}Pu and ^{240}Pu in a platelet of PuO_2 (a) and in a fibrous rod (b)

In the SIMS images, the white colour indicates the maximum concentration of the isotope that is normally in the middle of the particles.

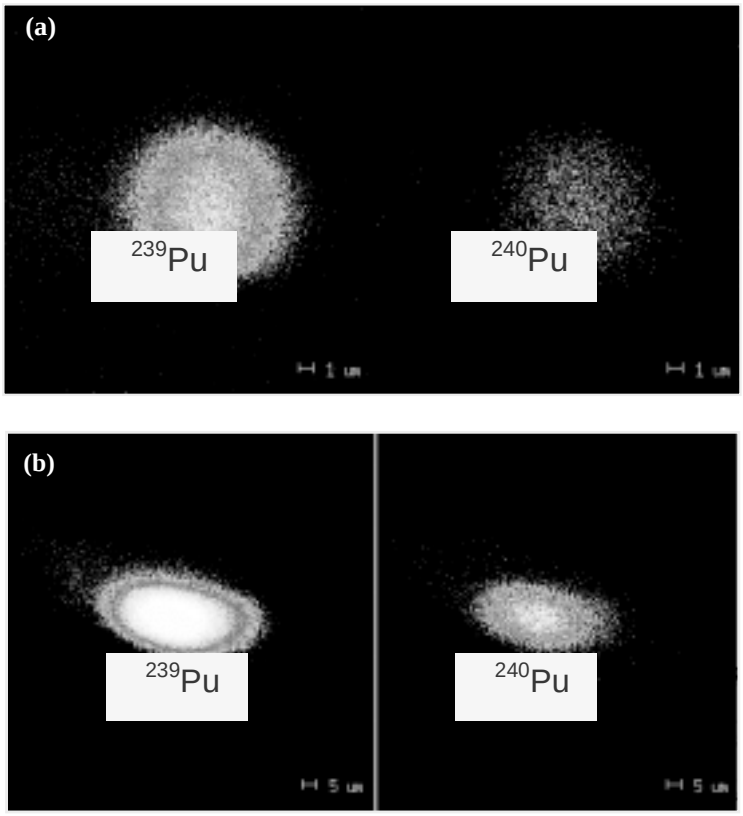

Acknowledgements

The authors are very grateful to the colleagues of the SEM laboratory (Dr. Ian Ray, Dr. T. Wiss and Mr. H. Thiele).

REFERENCES

[1] S.A. Durrani and R.K. Bull, "Solid-state Nuclear Track Detection: Principles, Methods and Applications", Pergamon Press, 71 (1987).

[2] L. Koch, I.L.F. Ray, M. Betti, A. Schubert, "Nuclear Forensics – The Investigation of Smuggled Nuclear Materials", ITU Annual Report, 26 (1998).

[3] G. Tamborini and M. Betti, "Application of Secondary Ion Mass Spectrometry for the Characterisation of Microparticles", *Mikrochimica Acta*, 132, 411 (2000).

[4] N. Erdmann, M. Betti, O. Stetzer, G. Tamborini, J.V. Kratz, N. Trautmann, J. van Geel, "Production of Monodisperse Uranium Oxide Particles and Their Characterization by Scanning Electron Microscopy and Secondary Ion Mass Spectrometry", *Spectrochimica Acta Part B*, 55, 1565-1575 (2000).

[5] M. Betti, G. Tamborini, L. Koch, "Use of Secondary Ion Mass Spectrometry in Nuclear Forensic Analysis for the Characterization of Plutonium and Highly Enriched Uranium Particles", *Analytical Chemistry*, 71, 2616 (1999).

HETEROGENEITY AND PHASE SEPARATION IN CRYSTALLINE SOLIDS MOSTLY CONTAINING PLUTONIUM

Steven D. Conradson, Francisco Espinosa-Faller, Phillip Villella
Materials Science and Technology Division, Los Alamos National Laboratory
Los Alamos, NM 87545, USA

Abstract

Within the last ten years, the once-contentious idea of local structural distortions as an intrinsic aspect of the arrangement of the atoms in crystalline materials and the complementarity of conventional diffraction methods and local structure techniques such as XAFS and PDF analysis have become standard tools in the structure determination box. However, we must now ask whether these advances go far enough or must our conceptual basis of crystal structure become even more radical if we are to accurately depict precisely how a crystal is assembled from its constituent atoms. Synchrotron X-ray measurements – both XAFS and X-ray PDF – on many different systems, but especially ones containing plutonium, show evidence for off-lattice atoms that exceed simple displacements or distortions. What we observe in these systems is most consistent with the formation of actual, relatively well-ordered alternative arrangements of the atoms that can involve up to one-quarter to one-third of the material but that do not diffract. One origin of this heterogeneity or phase separation will be composition fluctuations in non-stoichiometric materials. If a dopant is randomly distributed, the local fluctuations in its concentration will naturally tend towards a size just at or below the diffraction limit. A rearrangement of the atoms in these domains of different composition into a different structure will result in the observed effects. Furthermore, this local behaviour offers an explanation for correlated electronic and atomic effects in many of these materials, corroborating the idea of heterogeneity.

X-RAY MAGNETO-OPTICS IN LANTHANIDES AND PERSPECTIVES FOR STUDYING ACTINIDES

K. Starke, F. Heigl, A. Vollmer, G. Kaindl
Institut für Experimentalphysik, Freie Universität Berlin
Arnimallee 14, D-14195 Berlin-Dahlem, Germany

Abstract

Magneto-optical methods in the visible light regime generally lack element specificity, which has become a considerable shortcoming in research on advanced hetero-magnetic systems for storage technology. Here we review the recent discovery of magneto-optics in lanthanide materials [1] through which it has become feasible to study the element-specific magnetisation of lanthanides in hetero-magnetic compounds. To this end we employ circularly polarised soft X-rays in the energy regime of 100 eV, tuned to individual electric dipole $4d \rightarrow 4f$ transitions of lanthanide elements. We describe the experimental set-up and measurements of the element-specific magnetisation reversal of lanthanide films and nm-sized islands. In contrast to magneto-optics in the visible light regime, the temperature dependent X-ray magneto-optical signals from core-level transitions are not influenced by the thermal lattice expansion. Possible extensions of X-ray magneto-optics to higher photon energies and perspectives for studying magnetically ordered actinide systems are briefly discussed.

Introduction

Magneto-optical (MO) effects [2] are well known as the principle of how magnetic "bits" are read from an MO disk, where left and right-hand circularly polarised light is reflected with different intensity depending on the local disk magnetisation. In the visible-light regime MO effects are generally quite small. Yet refined optical methods yield sufficient contrast to not only distinguish between regions (bits) of opposite magnetisation, but even to observe details of magnetic domains in optical microscopes [3]. All MO techniques are ideally suited to study the magnetisation reversal process in external magnetic fields (hysteresis), which is impossible with many other techniques like, e.g. electron microscopes involving slow cascade electrons that are strongly affected by the Lorentz force.

Besides all merits, conventional MO techniques in the visible-light regime lack element specificity, simply because optical transitions in the visible take place between valence-electron band states which are spread over many lattice sites. Lacking element specificity has become a severe limitation in analysing modern materials for information storage [2,4] and small permanent magnets with nanometer dimensions [5]. Such advanced systems are composed of several magnetic elements to compromise technical requirements. In particular, lanthanide elements (mostly Tb) are used to reach a larger perpendicular magnetic anisotropy than usually obtained in 3d transition metal systems [6], or to achieve very large coercitive fields, e.g. in spring magnets [5].

Element-specific magnetic information can reliably be obtained by techniques which involve core level transitions, e.g. by magnetic circular dichroism in X-ray absorption (XA) [7,8]. In the soft X-ray range which is most relevant for magnetism studies, absorption signals are commonly detected by electron-yield methods [9], so that in general no large external magnetic fields can be employed. Hence no element-specific hysteresis loop (reaching typical coercitve fields in the kOe range) has ever been recorded via electron yield. There are alternative XA detection modes which do not employ electrons; yet they are either limited to special samples suspended on transparent foils [8], or they suffer from saturation effects for all but highly diluted samples (fluorescence yield) [10]. Thus, in order to probe magnetisation reversal in external fields in an element-resolved way, it appears natural to employ X-rays to reach core-levels and also to use light reflection as in conventional magneto-optics. Furthermore, the high X-ray penetration depth in low-Z elements, such as Be, allows one to use low-Z materials for sample protection, or as containment (e.g. Be cans) of radioactive materials [11].

Apart from their technological relevance in soft and hard magnetic films [5,6], lanthanide elements constitute a unique case in soft X-ray optics: the $4d \rightarrow 4f$ electric dipole transitions, so-called Giant resonances, are among the strongest in the periodic table [12]. They give rise to a high absorptivity and reflectivity, corresponding to an exceptionally short X-ray absorption length of $l \approx 1$ nm [13]. It is much shorter than the wavelength at which the lanthanide $4d \rightarrow 4f$ transition occurs ($\lambda \approx 8$ nm) representing the case $\lambda >> l$. This is quite different from $2p \rightarrow 3d$ transitions in Fe-like transition metals studied earlier [14,15], where attenuation lengths are much longer than the wavelength, $\lambda << l$, leading to complicated interferences for samples which are structured on the nanometer scale [15].

Experimental

The soft X-ray reflectivity experiments at the 4d-4f excitation thresholds of Gd and Tb (photon energy range: 130 eV-170 eV) have been performed in an ultra-high vacuum chamber (UHV, low 10^{-11} mbar range) using circularly polarised X-rays form the UE56 undulator beam line [16] at the synchrotron radiation source BESSY 2 at Berlin, Germany. As samples we prepared 1 nm-10 nm thin lanthanide metal films by *in vacuo* metal-vapour deposition onto a W(110) single-crystal substrate [17].

Figure 1 shows the W(110) coin-shaped single crystal mounted on a L-He flow cryostat (top centre) which allows a wide sample temperature range (between 20 K and 2 200 K). Magnetic fields up to 0.2 Tesla are applied through a (rotatable) horseshoe electromagnet. The reflected light intensity is measured using a standard Si photodiode; both photodiode and sample can be rotated about the same vertical axis, serving as a low-precision θ-2θ goneometer. The overall sample magnetisation was controlled *in situ* by standard (not element specific) magneto-optical Kerr effect (MOKE) using visible light.

Figure 1. Photograph of the wide temperature range W(110) sample holder (centre), placed inside a horseshoe electromagnet (fields up to 0.2 Tesla). Lower left: back side of a rotatable Si photodiode for in vacuum soft X-ray reflectivity.

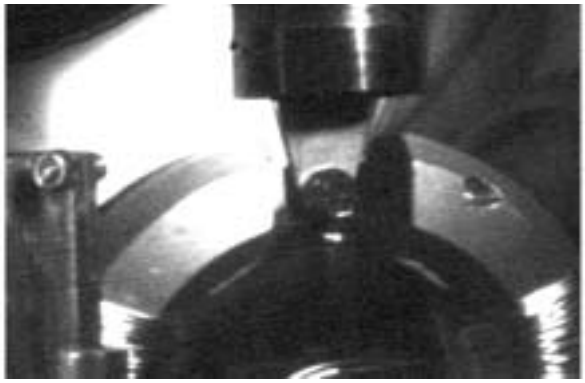

Results and discussion

As a first example we present absorption and reflectivity spectra of an in-plane magnetised 8-nm thick Gd metal film. Figure 2(a) (bottom) shows two Gd 4d $\rightarrow$ 4f absorption spectra, with the film magnetised either parallel (dotted) or anti-parallel (solid curve) to the projected direction of a beam of circularly polarised (CP) light. All spectral ranges change upon magnetisation reversal: the broad absorption maximum near $h\nu$ = 149 eV apparently shifts by some 1 eV, while energy and intensity of the much weaker pre-edge absorption lines change strongly [13]. The associated pair of X-reflectivity spectra in Figure 2(b) (above) is recorded from the same film in specular geometry; all spectra were recorded at θ = 18° grazing light incidence (see inset) and at T = 25 K sample temperature. For both magnetisation directions, there is a pronounced maximum of 20 times higher reflected intensity than at the minimum near 136 eV; the reflectivity maxima (solid and dotted curves) are located ~1.5 eV above the corresponding Giant absorption peaks [Figure 2(a)]. In the pre-edge range, only dispersive-like structures appear in reflectivity, with the points of steepest slope coinciding with the associated absorption peaks; this is nicely reflected by the almost isolated, lowest energy line magnified in Figure 2(c).

The shape of the reflectivity spectral features is well understood within elementary dispersion theory which formally describes the interaction of light with metals by introduction of a complex refractive index $\tilde{n} = (1 - \delta) - i\,k$ [18]. While for normally incident light both the absorptive part k and the dispersive part δ (deviation of the real part of $\tilde{n}$ from unity) contribute equally to the reflected intensity, the dispersive part clearly dominates at grazing incidence as is described by the Fresnel formulae [18,19]. Owing to the particularly short attenuation length l near the lanthanide 4d $\rightarrow$ 4f Giant absorption maxima, the difference in reflected light intensity upon magnetisation reversal is

Figure 2

(a) Gd 4d-4f absorption spectra obtained via electron yield from an 8 nm thick film with remanent in-plane magnetisation parallel (dotted curve) and anti-parallel (solid curve) to the (surface projected) incidence direction of a circularly polarised X-ray beam [inset of (b)].
(b) Associated spectra of specularly reflected light intensity.
(c) The lowest energy pre-edge structure at 139.2 eV in reflection (top) and absorption (below) [1].

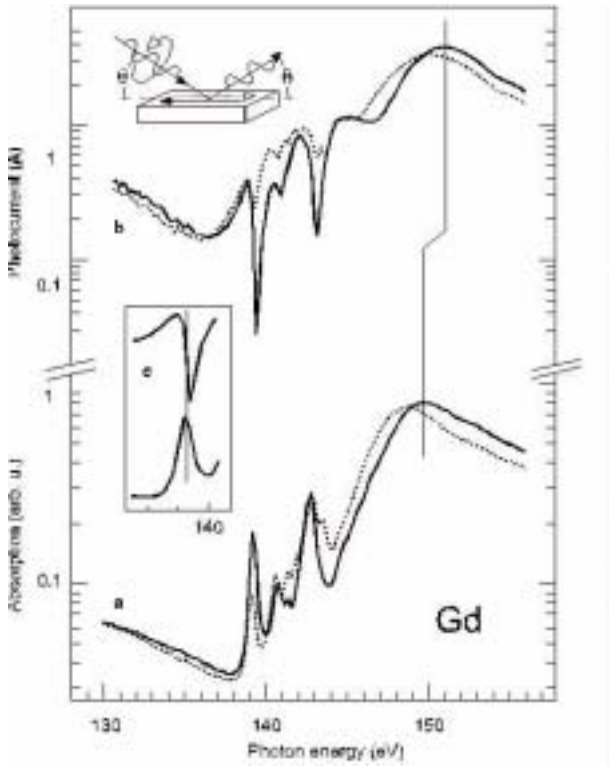

approximately proportional to the magnetisation, as long as the thickness *d* of the layer containing the absorbing element clearly exceeds *l*. This is quite different from previously investigated transition metals [15] involving 2p → 3d transitions (~20 nm attenuation length) where strong interference between individual magnetic layers has been observed in structures of a few nanometer size.

Unlike MO spectra in the visible-light regime involving valence-band transitions [2], 4d → 4f transition energies change significantly in going across the lanthanide series so that even neighbours in the periodic table such as, e.g. Gd and Tb can easily be distinguished. In Figure 3 we compare difference reflectivity spectra, obtained for opposite magnetisations of Gd and of an in-plane magnetised Tb film. The MO signal from Tb peaks near the Tb Giant absorption at hν = 157 eV, i.e. at several eV above the range of a substantial MO signal from Gd.

The energy separation between elemental MO signals at the lanthanide 4d-4f threshold allows one to record element-specific hysteresis loops from hetero-magnetic systems. As a first demonstration we fabricated a $Gd_{1-x}Tb_x$/Gd nanostructure, prepared by annealing of a 0.3 nm Tb layer deposited on top of a ~3 nm thick Gd film on W(110) at 1 070 K; at such a high temperature, the metastable film is expected to break up into large three-dimensional islands [20]. Figures 4(a) and 4(b) present hysteresis loops recorded at two different photon energies, 147 eV and 153 eV. By inspection of Figure 3, we identify 147 eV with the maximum of the Gd spectrum and with a node in the Tb spectrum (energy 1); the 147 eV hysteresis loop in Figure 4(a) thus reflects the magnetisation reversal of the Gd atoms only.

Figure 3

(a) Difference spectrum obtained from the Gd 4d → 4f reflectivity spectra in Figure 2(b).
(b) 4d → 4f difference spectrum of reflected intensity from an 8 nm thick Tb metal film (T = 25 K). Photon energies 1 and 2 are used to record hysteresis loops (Figure 4) [1].

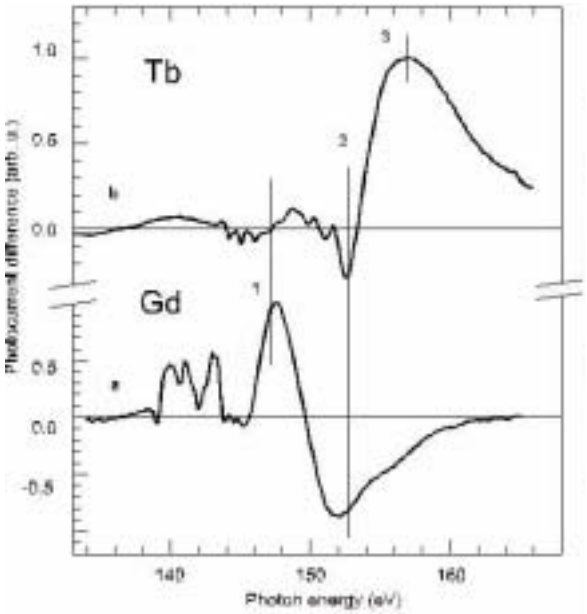

The loop shows two magnetically different Gd species, a magnetically soft one with low coercivity (80 A/cm) and another one in which magnetisation reverses at a five times higher external field (400 A/cm). The overshoot clearly reveals that Gd moments in these two phases are oriented parallel to each other for increasing fields between the two coercivities, but anti-parallel to each other in high external fields – a quite surprising behaviour at first glance. The 153 eV hysteresis [Figure 4(b)] comprises MO signals of both elements (see point 2 in Figure 3). Like the 147 eV loop, it indicates that the magnetisation reverses in two steps, yet there is no overshoot. Assuming the absence of interference effects as was discussed above, we obtain the shape of the magnetisation-reversal curve of Tb simply by subtracting the 147 eV loop (Gd) from the one at 153 eV (superposition of Tb and Gd), with the result given in Figure 4(c).

From the element-specific Gd hysteresis [Figure 4(a)] and the difference loop in Figure 4(c), which we identify with the magnetisation reversal of Tb atoms, we conclude: (1) It is the presence of Tb which gives rise to the magnetically harder Gd phase. (2) The orientation of Gd 4f-moments (at high fields anti-parallel to the external field) is due to an anti-ferromagnetic coupling of Gd and Tb moments in the magnetically hard Gd phase. The hard phase is tentatively assigned to a $Gd_{1-x}Tb_x$ alloy, in which the larger Tb 4f moment (9 μ_B) dominates over the Gd 4f moment (7 μ_B) and points along high external fields, see dashed arrows in Figure 4(b). Note that the low-coercivity Gd, which we identify with the metallic (not alloyed) phase, is not magnetically coupled to the hard magnetic phase; this observation is consistent with the expected separated-island structure of the film.

Another principal difficulty of visible-light MO spectroscopy concerns thermal changes of non-magnetic origin: valence-band energies slightly change with the thermally expanding lattice, which affects the optical constants and thus the reflected intensity of visible light. This complication impedes in many cases a magneto-optical measurement of magnetisation-versus-temperature curves, $M(T)$. By contrast, lanthanide 4d → 4f transitions only involve core levels which do not take part in

Figure 4

(a) Hysteresis loops of a $Gd_{1-x}Tb_x$/Gd nanostructure at different photon energies. At 147 eV, changes in the reflected light intensity are solely due to Gd. The loop reveals two magnetically different Gd phases, a low-coercivity one (Gd metal) and a magnetically harder phase ($Gd_{1-x}Tb_x$ alloy). The associated magnetic orientations are indicated by big and small solid arrows, respectively.

(b) The 153 eV loop reflects magnetisation changes of both elements. The Tb magnetisation is indicated by dashed arrows at different stages of the magnetisation reversal process.

(c) The difference of the loops in (b) and (a) is interpreted as the shape of the Tb hysteresis [1].

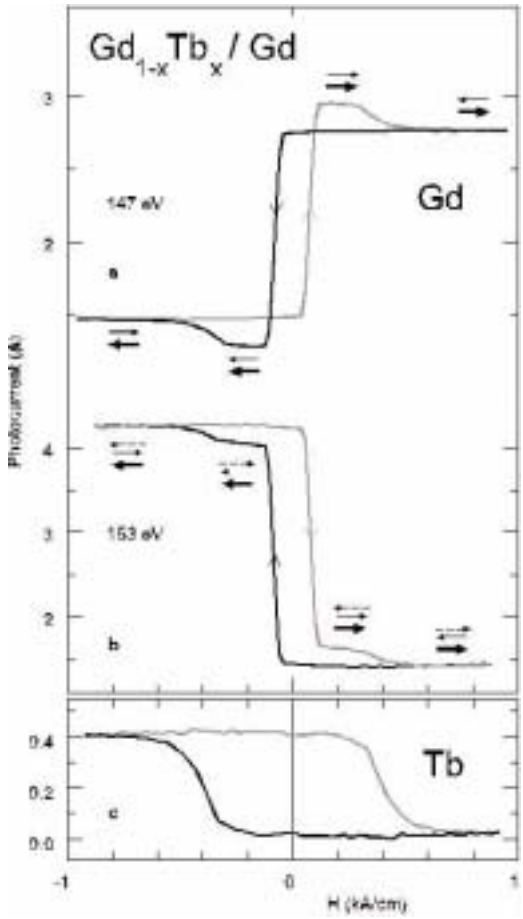

chemical bonding, and we may anticipate that 4d → 4f transition intensity changes reveal only changes in the 4f magnetisation. Figure 5(a) demonstrates that this is indeed the case. A Tb film was cooled, from above room temperature where it is paramagnetic to ~20 K, in the presence of an external magnetic field of 1 kA/cm applied along the film plane, while recording the specular intensity at 157 eV (compare with Figure 3). Above the ordering temperature (Neel temperature T_N) of 220 K, which is reduced as compared to the bulk value (232 K) owing to the small sample thickness (8 nm), the reflected intensity remains constant and it is independent of the field direction. Below T_N it steeply rises (drops) when the field is parallel (anti-parallel) to the projected light propagation direction. As is well known from previous analyses of bulk samples [21], we find that a helical magnetic phase exists within a few Kelvin below the ordering temperature; it has been suppressed by the external field (1 kA/cm). The difference in reflected intensity [Figure 5(b)] amounts to several μA of photocurrent which is easily measured with high accuracy. Such accurate $M(T)$ data provide access to fundamental magnetic quantities such as, e.g. the critical exponent of the magnetisation β, defined through

Figure 5

(a) Temperature-dependent reflectivity curves of an 8 nm thick Tb film, cooled down in external magnetic fields of opposite directions (dotted and solid curves). The constant reflectivity in the paramagnetic temperature regime demonstrates that 4d → 4f core-level transitions are not affected by non-magnetic thermal effects.

(b) Magnetisation curve M(T), which is the difference of the two curves in (a).

(c) Double logarithmic plot of the Tb film magnetisation as a function of the reduced temperature $t = (1 - T/T_C)$. The critical exponent $\beta = 0.31 \pm 0.02$ is determined by a least-squares fit analysis in the range $1 \cdot 10^{-2} < t < 8 \cdot 10^{-2}$ [1].

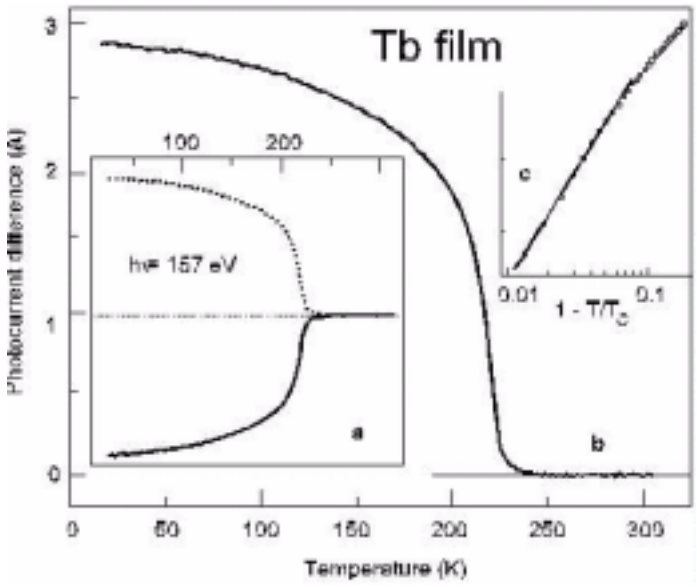

$M(T)/M(0) = (1 - T/T_C)^{\beta}$. For comparison we measured the Tb film magnetisation also by standard MOKE using visible light (λ = 633 nm). As expected, both methods yield the same $M(T)$ behaviour of the Tb magnetisation; however the visible-light MOKE data show a substantial temperature variation of non-magnetic origin which we attribute to thermal lattice expansion [22].

A closer inspection of the critical regime just below the ordering temperature in Figure 5(c) yields a critical exponent $\beta = 0.31 \pm 0.02$. It agrees with the theoretically expected value for a three-dimensional Ising system, indicating the presence of a substantial considerable magnetic anisotropy in the Tb metal film; the latter is likely to be induced by the bcc W(110) substrate of uniaxial symmetry.

Summary and perspectives

The discovery of large and easy-to-measure magneto-optical signals in the soft X-ray regime opens several new avenues in magnetism research. *(1)* Intense X-ray beams from third-generation synchrotron radiation sources can be focused down to a few 10 nm spot size by Fresnel zone plates, utilised in several X-ray microscopes world-wide. So far a magnetic resolution of ~60 nm has been obtained using transparent samples suspended on organic foils [23]. MO signals in reflectivity from lanthanides at the 4d → 4f threshold will now allow element-specific microscopy studies on technically relevant non-transparent metal or semiconductor substrates, e.g. on the currently most relevant question concerning the switching behaviour of heteromagnetic nanoscale systems [4,5]. *(2)* The XMOKE method can be extended into the hard X-ray regime, employing CP light excitation at lanthanide 3d → 4f thresholds [24] and at 3d → 5f thresholds of actinide systems ($M_{4,5}$ edges).

A remarkable 3d $\rightarrow$ 5f resonance enhancement of the magnetic X-ray scattering cross-section by 10^7, as compared to off-resonance scattering, has been observed at the M_4 edge of uranium compounds [25]. It has been applied to a first X-ray scattering study of magnetic structures near the surface of UO_2 [11]. Although pronounced resonance enhancements should also be expected at the shallower actinide nd $\rightarrow$ 5f thresholds [26], measurements at $M_{4,5}$ edges might be most convenient since low-Z containment materials become transparent at higher photon energies (U M_5: 3.55 keV)

Acknowledgements

The authors are indebted to the staff of BESSY II for their co-operation in the preparation and performance of the experiments at the U56/1-PGM. This work was supported by the BMBF, project 05-SC8 KEB-6 and the DFG, Sfb290/TP A06.

REFERENCES

[1] K. Starke, F. Heigl, A. Vollmer, M. Weiss, G. Reichardt, G. Kaindl, *Phys. Rev. Lett*., submitted April 2000.

[2] S. Sugano and N. Kojima, *Magneto-Optics* (Springer, Berlin, Heidelberg, 2000); D.S. Bloomberg and G.A.N. Connell in *Magnetic Recording Handbook: Technology and Applications*, C.D. Mee, E.D. Daniel, eds., (McGraw-Hill, New York, 1990).

[3] A. Hubert and R. Schäfer, *Magnetic Domains* (Springer, Berlin, Heidelberg, 1998).

[4] G.A. Prince, *Science*, 282, 1660 (1998).

[5] J.S. Jiang, *et al*., *J. Appl. Phys.*, 83, 6238 (1998); S.A. Majetich, Y. Jin, *Science*, 284, 470 (1999).

[6] D. Weller and W. Reim, *Appl. Phys. A*, 49, 599 (1989); Y. Takeno, K. Kaneko, Y. Shimada, *J. Magn. Soc. Jpn.*, 19, S229 (1994).

[7] G. Schütz, *et al*., *Phys. Rev. Lett.*, 58, 737 (1987).

[8] C.T. Chen, *et al*., *Phys. Rev. Lett.*, 75, 152 (1995).

[9] J. Stöhr and R. Nakajima, *IBM J. Res. Develop.*, 42, 73 (1998).

[10] L. Tröger, *et al*., *Phys. Rev. B*, 46, 3283 (1992); C.T. Chen, *et al*., *ibid.*, 48, 642 (1993).

[11] G.M. Watson, D. Gibbs, G.H. Lander, B.D. Gaulin, L.E. Berman, Hj. Matzke, W. Ellis, *Phys. Rev. Lett.*, 77, 751 (1996); *Phys. Rev. B*, 61, 8966 (2000).

[12] B.L. Henke, E.M. Gullikson, J.C. Davis, *Atomic Data and Nucl. Data Tables*, 54, 180 (1993).

[13] K. Starke, *et al*., *Phys. Rev. B*, 55, 2672 (1997); *Eur. Phys. J. B*, 12, 171 (1999).

[14] H.A. Dürr, *et al*., *Science*, 284, 2166 (1999).

[15] C-C. Kao, *et al*., *Phys. Rev. B*, 50, 9599 (1994); Y.U. Idzerda, V. Chakarian, J.W. Freeland, *Phys. Rev. Lett.*, 82, 1562 (1999).

[16] K.J.S. Sawheney, *et al*., *Nucl. Instr. Met. A*, 390, 395 (1997).

[17] K. Starke, *Magnetic Dichroism in Core-level Photoemission* (Springer, Berlin, Heidelberg, 2000), Sect. 3.

[18] M. Born and E. Wolf, *Priciples of Optics* (Pergamon, London, 1959).

[19] A semiquantitative description of the reflected light intensity in both, the pre-edge and the Giant resonance range is given in Ref. [1].

[20] E.D. Tober, *et al*., *Phys. Rev. B*, 53, 5444 (1996).

[21] J. Jensen and A.R. Mackintosh, *Rare Earth Magnetism Structures and Excitations* (Clarendon, Oxford, 1991), Sect. 5.7.

[22] F. Heigl, G. Kaindl, K. Starke (unpublished).

[23] P. Fischer, *et al*., *Z. Phys. B*, 101, 313 (1996).

[24] Z. Hu, *et al*., *Phys. Rev. B*, 59, 9737 (1999).

[25] E.D. Isaacs, D.B. McWhan, C. Peters, G.E. Ice, D.P. Siddons, J.B. Hastings, C. Vettier, O. Vogt, *Phys. Rev. Lett.*, 62, 1671 (1989).

[26] G. Kalkowski, G. Kaindl, W.D. Brewer, W. Krone, *Phys. Rev. B*, 35, 2667 (1987).

THE PRESSURE BEHAVIOUR OF ACTINIDES VIA SYNCHROTRON RADIATION

R.G. Haire,[1] **S. Heathman,**[2] **T. Le Bihan**[3] **and A. Lindbaum**[4]
[1]Oak Ridge National Laboratory, Oak Ridge, TN 37831-6375 USA
[2]Institute for Transuranium Elements, Karlsruhe, German
[3]European Synchrotron Radiation Facility, Grenoble, France
[4]Institute for Experimental Physics, Vienna University of Technology, Austria

Abstract

Various aspects of performing high-pressure studies with radioactive f-elements using synchrotrons as sources of X-rays are discussed. For ultra-high pressures, intense well-focused beams of 10 to 30 microns in diameter and a single wavelength of 0.3 to 0.7 Å are desired for angle dispersive diffraction measurements. Special considerations are necessary for the studies of transuranium elements under pressure at synchrotron facilities. Normally, with these actinides the pressure cells are prepared off-site and shipped to the synchrotron for study. Approved containment techniques must be provided to assure there is not a potential for the release of sample material. The goal of these high-pressure studies is to explore the fundamental science occurring as pressure is applied to the actinide samples. One of the primary effects of pressure is to reduce interatomic distances, and the goal is to ascertain the changes in bonding and electronic nature of the system that result as atoms and electronic orbitals are forced closer together. Concepts of the science being pursued with these f-elements are outlined. A brief discussion of the behaviour of americium metal under pressure performed recently at the ESRF is provided as an example of the high-pressure research being performed with synchrotron radiation. Also discussed here is the important role synchrotrons play and the techniques/procedures employed in high-pressure studies with actinides.

Introduction

Electromagnetic radiation has long been employed for characterising materials, and third-generation synchrotrons offer unparalleled opportunities in this regard. In the area of X-ray diffraction, a classical tool for structural determinations, synchrotrons offer not only a very intense X-ray source but also provide beams of superior dimensions and stability that can be readily customised. These are the characteristics that have greatly expanded the ability to perform ultra-high pressure research, and have attracted researchers wishing to investigate actinides under pressure at synchrotron facilities.

There has been increased interest in the effects of pressure on f-elements and compounds, especially as pressures in the megabar region are now easily attainable. An important issue in these studies is to determine how the decreasing interatomic distances, brought about by applying pressure, can effect the electronic nature and/or bonding in these materials. Specifically, for the f elements, the question is whether such changes effect the normally non-bonding (localised) f electrons themselves and incorporated them in some manner into the bonding of the materials. The 5f electrons of the actinide elements, which are all radioactive to varying degrees, are particularly intriguing in this regard.

Whereas it is accepted that the actinide elements from protactinium through plutonium have f electrons involved in their bonding at normal pressure, in contrast the transplutonium elements are considered to be more lanthanide-like and do not. Thus, one goal for investigating transplutonium metals is to determine if pressure can bring about delocalisation of their f electrons and thereby alter the nature of the bonding in the materials.

The spatial extent of the 5f electrons is greater than that of the 4f electrons, and close in energy to the 6d, 7p and 7s electrons. Altering certain parameters, such as pressure, may then change the total energy of the system. An especially interesting element in this regard is americium (element 95), the near neighbour of plutonium (element 94). At room temperature and pressure, plutonium is accepted as having overlapping orbitals, which involve its 5f electrons (hybridised band structure), while americium has localised 5f electrons (e.g. 5f electrons in a narrow region). The question becomes whether pressure can reverse this sudden change in 5f electron behaviour that is observed in this region of the actinide series. That is, can pressure cause the 5f electrons of americium to participate in the bonding? There is also interest in the behaviour of different actinide compounds and alloys under pressure. These latter materials present an additional complexity in that more than one kind of atom is involved.

Structural information in high-pressure studies is basically obtained in the classical manner using X-rays, except that a diamond anvil cell (DAC) is employed for applying pressure on the sample. The DAC imposes some restrictions in the diffraction studies, but the nature and flexibility of the synchrotron radiation makes it the preferred choice for pressure work, especially at the higher pressures. There are several obvious advantages to using synchrotron radiation for pressure studies, but for pressures of one or more megabars, the small (10-30 micron diameter) X-ray beams of high intensity are very significant, in some instances even being a necessity.

This work will cover different aspects, both positive and negative, of performing high-pressure studies with radioactive f elements at synchrotron facilities. The important role synchrotrons play in studies with actinides, together with the needs and responsibilities of scientists performing such investigations will also be addressed. Some of the science being pursued with actinides will be outlined and demonstrated by a brief discussion of selected studies, which includes the investigation of americium metal under pressure recently performed at the ESRF (Grenoble, France).

Experimental aspects

Materials

The actinide elements are all electropositive metals and display variable reactivity toward water and air. They are prepared by various techniques [1-3], depending on their particular physicochemistry and availability. In experiments with the limited quantities of the element and with isotopes having short half-lives, the preparation of the metals becomes an integrated part of the high-pressure studies. Reactivity of the metal is a concern, especially considering the small amounts of the sample employed in the high-pressure study. In most cases, sample loading of the DAC must be performed in inert atmosphere glove boxes to protect the sample from moisture and air, as well as to provide containment for the radioactive materials. Thought must also be given to the pressure-transmitting medium being used, to assure that it will not bring about sample degradation, especially with a lengthy transportation period. Generally, silicon oil and liquefied gases (Ar, He, N_2, etc.) are acceptable, whereas alcohol (e.g. mixtures of methanol and ethanol) can react with some actinide metals, especially those with higher radiation fields that decompose the alcohol to more reactive products.

Diamond anvil cell

There are a number of diamond anvil cell (DAC) designs and it is not the purpose here to compare them. Nor is there an attempt to discuss the preparation of loading/unloading techniques employed. Rather, the discussion is aimed at operations necessary to allow radioactive samples in a DAC to be studied at a synchrotron.

In this work we employed three cell designs:

- Cornell design [4].
- Syassen-Holzapfel design [5].
- Megabar design [6].

The first design is best suited for pressure of a megabar or more, whereas the second design is limited to pressures of ~ 60 GPa. The DAC by necessity (for alignment, installation of parts, etc.) has several openings to the diamond anvil area. These openings must be “sealed” when using radioactive samples at a synchrotron. The diamonds and gasket provide the first level of containment. In addition, other containment must also be provided. For the latter perspective, some cell designs are more adaptable than others. We have found that the Cornell DAC design lends itself nicely for such containment. A photograph of two views of the Cornell cells is shown in Figure 1.

This DAC is essentially a precision-bored, block of stainless steel that contains a fixed diamond anvil and is fitted with a movable piston containing a matching diamond anvil. The piston is associated with the large nut on the right side of the left-hand cell in Figure 1. The accesses through the block are sealed with oval aluminium plugs (threaded hole in centre) and a second Allen screw in each corner. A brass piece fitted with a 6 mm diameter beryllium window is screwed and sealed into the movable piston (visible only as a nut on the left cell), and rests just before the base of the diamond. The X-ray beam enters the piston opening and then passes through a beryllium window. After passing through this window, the movable diamond, the sample and the fixed diamond, the X-rays exit pass through the end slit.

Figure 1. Two Cornell-type diamond anvil cells with special containment pieces for studying radioactive samples (a beryllium window inside of the housing of the movable piston is not shown)

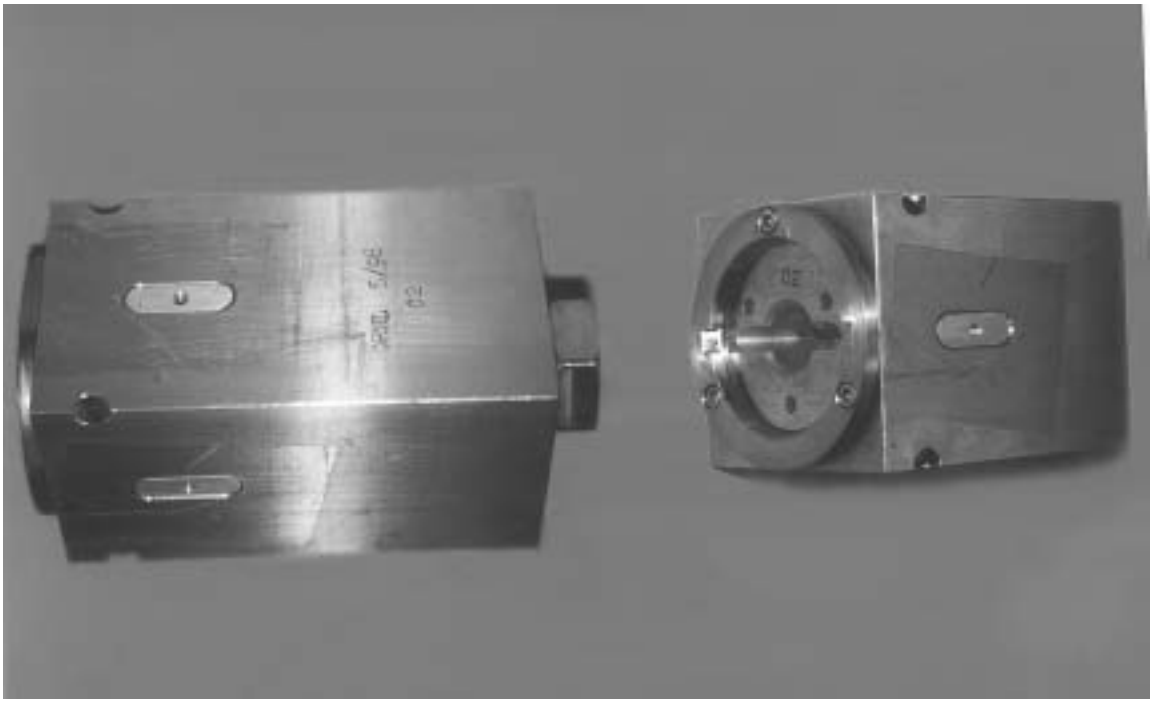

The exit slit is visible in the right hand cell (Figure 1) and provides limited two-theta angle of some twenty degrees. The exit slit is fitted with a large brass ring which has a high strength plastic (Melinex®, a polyester film by Dupont) sealed to it. The ring is held on the DAC by three screws. The plastic window was chosen both for its strength and its ability to transmit the ruby's fluorescence, when the latter is used for pressure determination. Either ruby fluorescence or the equation-of-state for platinum were the techniques used for the pressure determination. Using a plastic film over an aluminium frame also provided additional containment for the cell.

Containment for the other two cell designs was similar in principal, through both were more difficult given the different cell constructions. Containment for these two cell designs is not discussed here, but a similar approach was used for the other cells.

Special techniques have been developed for loading/unloading the DAC at ORNL. Experience has shown these cells can be loaded with radioactive samples, used in the studies and then unloaded without contaminating the DAC, except for the gasket and diamond surfaces. It has been found that the diamonds can easily be de-contaminated and re-used in other studies.

DAC and synchrotron radiation

High-pressure studies with a DAC can employ either energy dispersive or angle dispersive techniques. Both techniques have advantages and disadvantages but overall we have preferred the angle dispersive technique for studies with synchrotron radiation. This approach provides excellent resolution, most flexible operational conditions, and given the high intensity of the radiation, does not suffer with regard to the collection time for the diffraction data. Angle dispersive studies with a DAC do have some special requirements, and these vary with the properties of the specific cells being used.

A few comments relative to the study of f-elements in a DAC at synchrotrons are provided here. With the angle dispersive technique, X-rays of a wavelength shorter than ~0.7 Å (e.g. 0.7-0.3 Å) are used to maximise the diffraction data that can be collected. A wavelength of 0.7 Å is sufficient to pass through the two diamonds and the sample. Shorter wavelengths allow "compressed" diffraction data to be collected to favour higher angles. Altering the sample to detector distances and/or rotating the cell relative to the beam are other approaches that can be undertaken at advanced facilities. These techniques help overcome the limitation of having relatively small diffraction angles provided by the DAC (~20-25 degrees 2 Θ). Finally, the rapid image plates and readout used at the ESRF facility are very important, and allow complete diffraction patterns to be obtained with the synchrotron radiation in less than a minute.

The superiority of synchrotron radiation for high-pressure studies with actinides is in the machine's ability to provide intense, well-focused and stable X-ray beams with of 10-30 microns in diameter. As the desired pressure region for the studies increases, there is a need for smaller diamond anvils, small gasket openings and smaller sample sizes. In many cases, diamond anvils with 70-100 micron surfaces and having a gasket with 30-60 microns in diameter opening are used; only a few micrograms of actinide sample are employed. These conditions require the small, intense X-ray beams provided by synchrotrons in order to perform a complete study of the material at very high pressures in the allotted experimental time.

Specifically, the experimental procedure often uses micro-focused beams of nominally 25×25 μm (two bent mirrors in conjunction with a 30 μm pinhole filter) in many of the studies. Under these conditions, a 15-second exposure is sufficient (2/3 fill machine mode, at 200 mA) to yield excellent diffraction images. The images are captured with a Fastscan image detector [7] and can be viewed in 15-60 seconds. This allows a large number of diffraction images to be collected in a short time.

Presently, facilities are not available at synchrotrons for loading and preparing DAC with radioactive samples, although facilities exist for preparing certain types of samples at the synchrotron. For high-pressure studies, it is required that the DAC samples be loaded, prepared for study at a synchrotron site and then transported to that site by official carriers. This transportation is costly, time consuming and the process is not forgiving if the sample is unsatisfactory upon arrival.

This transportation process also limits the number of samples and increases the inability to successfully study a particular sample. The DAC is an expensive sample device and only a limited number are normally available at one time. Transportation itself limits the number of cells that can be transported at one time. Thus, the experimenter must choose between having different samples or having one or two materials with back-up samples. The total number of samples often falls into a range of one to six in these high-pressure synchrotron studies with actinides.

f-elements under pressure

Over the past few decades there have been several studies of the lanthanides and actinides under pressure. Given recent advancements in high-pressure work and the use of synchrotrons, higher pressures have been attained and new concepts concerning behaviour under pressure have been formed. The reader is referred to reviews [8-11] on high-pressure studies with f-elements and recent work on Ce metal [12]. There is strong evidence that the 4f electrons in the lanthanide series delocalise under pressure and that these metals adopt low-symmetry structure types known for the Pa-Pu metals, which normally have itinerant f electrons. The pressure for this delocalisation process increases as one moves across the lanthanide series (as the f electrons are "pulled in" by the greater nuclear charge);

it has not been reported for members of the second half of this series. The greater spatial extension of the 5f electrons in the actinides, as compared to the 4f electrons in the lanthanides, is expected to permit the delocalisation process in the former to occur at lower pressures.

The physicochemical properties of the actinide metals at normal pressure vary considerably across the series. This is largely due to the changing role of the 5f electrons. It is accepted that the 5f electrons in the protactinium through plutonium metals are involved in bonding at normal temperature and pressure, and these metals display quite different properties than the lanthanide or transplutonium metals. The 5f electrons of the transplutonium metals are localised and their behaviour is more like that of the lanthanide metals. In this regard, americium metal is in a pivotal position in the series and its behaviour under pressure is especially interesting. The determination of whether pressure can bring about this delocalisation is an important aspect of DAC studies with transuranium elements.

The concept of identical homologues between the lanthanide and the actinide metals is seriously limited, especially in terms of their pressure behaviour, although some comparisons/relationships are valid and useful. In these pressure studies using X-ray diffraction, the approach is to monitor the structure of the metals as a function of pressure and extract the bonding behaviour from established structure-bonding relationships. These structure-bonding relationships have both an experimental and theoretical basis. The goal is to use both theory and experiment to understand the pressure behaviour and to promote the convergence of experimental and theoretical views of the metals under pressure.

There are at least two different processes envisioned for the 5f electrons when the metals are subjected to pressure. One effect is for the 5f electrons to combine/overlap with other electron orbitals to form a hybrid-type of bonding band (as exists with the Pa-Pu metals at normal pressure). In essence, the 5f electrons become delocalised and become involved in bonding, either totally or partially. In this situation, it would be expected that lower symmetry structures would form, perhaps similar or identical to the structures exhibited by the protactinium through plutonium metals.

The second process is for the pressure to cause promotion of the f-electron to another state (e.g. f $\rightarrow$ d) and then this new state would become involved in bonding. This does not seem to have been observed experimentally in pressure studies to date. A potential example would be to apply pressure on divalent einsteinium metal ([Rn core] $5f^{11}$ $7s^2$) and force it to become trivalent einsteinium metal ([Rn core] $5f^{10}$ spd). Simple calculations indicate this could occur at relatively lower pressures.

The primary structural effects of pressure are: dynamic compression, structural transformations and volume collapses. In many of the structural transformations involving high symmetry, common metal structures, s-d interactions are the driving force, as the relative energies of these orbitals change with pressure. Transformation from a high to lower symmetry structure can suggest potential incorporation of f-electron character. A sudden volume collapse is indicative of the onset of f-electron involvement.

The above discussion provides a snapshot of what investigations of actinide metals under pressure are pursuing in high-pressure studies at synchrotrons. The studies require the application of established structure-bonding concepts and relationships. Other complimentary analysis under pressure would of course be useful/informative, and some have been done at lower pressures. However, the situation is that these other analytic probes (magnetism, resistivity, etc.) are far more limited in the pressures that can be obtained. The DAC probably provides the highest pressure that can be experimentally obtained in static measurements. The types of changes being pursued very likely require these high pressures.

In the subsequent section, important aspects of americium's behaviour under pressure, determined in recent studies at the ESRF [13], will be discussed. Studies of americium under pressure have been reported previously at lower pressures using conventional X-ray radiation sources. The recent work on americium [13] differs significantly in the structures observed in the mid- to high-pressure regions, and these new findings were made possible through the use of synchrotron radiation.

Recent studies on americium metal

Americium metal was studied recently at the ESRF high-pressure diffraction facility (ID30) and the initial findings reported [13]. These studies greatly extended the pressure range examined previously, from 60 GPa to the reported limit of 100 GPa. In addition, the high quality (resolution) and extensive diffraction data acquired at the ESRF resolved previous disagreements about the high-pressure behaviour of americium. These new data have allowed a new understanding of the behaviour of americium under pressure. These data are shown in graphical form in Figure 2 as a plot of relative volume (volume at pressure/volume at normal pressure) versus pressure. The insert in the figure displays the atomic volume of the different actinide metals versus the atomic number, showing the sharp increase in volume in going from plutonium to americium. This increase reflects the change from having delocalised electrons in plutonium (smaller than expected atomic volume) to having localised f electrons found in americium. If the localised f electrons in americium suddenly became delocalised (e.g. by applying pressure), a sharp reduction in its atomic value would be expected (e.g. the volume for americium in the insert would drop down toward the volume shown for plutonium). Conversely, if f-electron involvement could be removed in α plutonium (generation of localised f electrons), its volume should increase towards that of americium. This can be partially accomplished by heating or alloying of plutonium with small amounts of other metals.

Figure 2. Relative volume versus pressure curve for americium metal

Inset shows the atomic volume of the actinides as a function of element

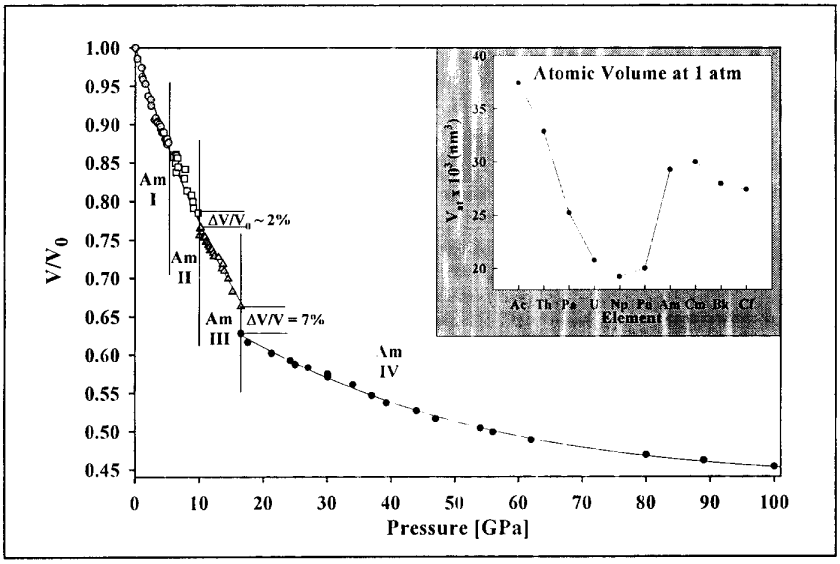

Figure 2 displays that four phases were observed for americium metal under pressure in a recent study [13] at the ESRF. Previous researchers have reported data and interpretations about the behaviour of americium metal under pressure below 60 GPa [14-21]. The main differences in Figure 2 from earlier work are found in the two phases labelled Am(III) and Am(IV). Differences included both the

structural assignments and the transition pressures for these two phases. In addition, a second, small volume collapse was observed for the first time at the transition between the Am(II) and Am(III) forms (Figure 2).

The structures observed for the four forms were: Am(I) – dhcp (P63/mmc); Am(II) – fcc (Fm3m); Am(III) – orthorhombic (Fddd) and Am(IV) – orthorhombic (Pnma). The Am(IV) form is similar to the α uranium type structure (Cmcm) [13], while the Am(III) structure is isostructural with an elevated temperature form of plutonium metal (γ plutonium). Both the Am(III) and the Am(IV) structures are believed to involve f-electron character, as do α plutonium and α uranium. A detailed discussion and experimental information can be found in the paper [13]. The results of the pressure study on americium metal can be looked at as a form of "modern structural alchemy". Under pressure americium (II) adopts first the structure of γ plutonium and then a structure with a "slightly altered" arrangement of the atoms than found in α uranium (loosely speaking, a slightly altered form of α uranium). The structures are displayed graphically in Figure 3, where the arrangement of the americium atoms in each form and the transformation processes between structures can be visualised.

Figure 3. A form of modern alchemy

Under high pressure, americium [Am(II)] first adopts the structure of γ plutonium [Am(III)] and then a structure that is "slightly altered" from that of α uranium [Am(IV)]

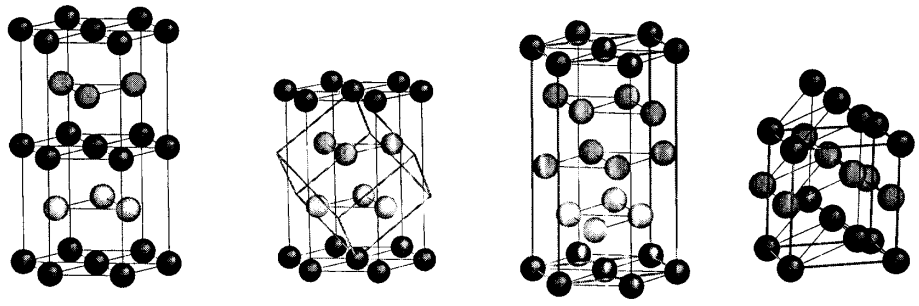

The ability to resolve the behaviour of americium under pressure was the result of the high quality of the diffraction data obtained at the ESRF synchrotron facility. The quality of these data was confirmed in Rietveld analyses of the data at different pressures, and Bragg-R factors of 5-8% were obtained for the derived structures. The results of the refinements for some data sets for the face centred orthorhombic Am(III) and primitive, orthorhombic Am(IV) structures are shown in Figure 4. The space group for the Am(III) structure is Fddd and that for the Am(IV) structure is Pnma. The latter space group has a lower symmetry than the Cmcm space group for α uranium, which itself is a complex structure.

Summarising comments

The attributes of synchrotron radiation have permitted and hopefully will continue to advance the high-pressure science of the actinides. Obtaining high-quality diffraction data is crucial to ascertain the proper structural behaviour from which electronic and bonding nature of the material is extracted. Synchrotron radiation is very important when ultra-high pressures are sought, as it can provide the characteristics and the very critical beam conditions that are required for these particular DAC investigations. The flexibility and variability of the beams from modern synchrotrons are additional benefits.

Figure 4. Rietveld fits for the Am(III) and Am(IV) structures at 10.9 and 17.6 GPa

Shown are experimental (dark lines) and calculated (grey lines) diffraction patterns, reflection tick marks and difference profiles (bottom line) [13]

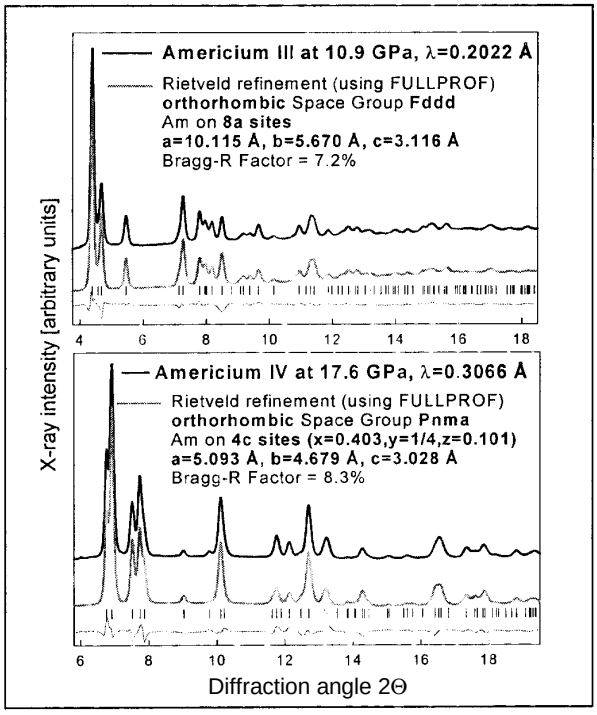

Drawbacks to high-pressure studies with actinides at synchrotrons are the lack of on-site facilities for loading/unloading the DAC. These are not likely to be available, especially in the near term, given the requirements for handling DACs, as well as more extensive work needed with radioactive materials in DACs. In the absence of such facilities, it is necessary to transport the DACs pre-loaded with sample and contained. This can be expensive, difficult and time-consuming, and the transport of radioactive materials is not likely to become easier in the future. This situation is made even less attractive by the fact that researchers are likely to have only a limited number of DACs for transportation at any one time. This reduces the number of samples that can be available for study during a particular allotment of beam time. In many instances, a choice must be made between having a back-up sample or another sample material for study.

The potential for new advancing actinide science is good for these high-pressure studies. In condensed matter studies, the large reductions in interatomic distances attainable with pressure are much greater than increases in such distances acquired by temperatures for conditions attainable in the laboratory. Hence, important changes can be induced in the bonding and physicochemical changes in actinide metals and compounds by applying pressure.

The recent studies of americium metal using synchrotron radiation provides an example of the type of new information that can be obtained with modern techniques. Properly identifying the Am(III) and Am(IV) pressure phases in recent studies at the ESRF allowed new insights to be obtained into the behaviour of 5f electrons both under pressure and at normal pressure. Observing a partial delocalisation of americium's 5f electrons in the Am(III) phase to form a γ plutonium type structure followed by a second delocalisation step is perhaps the first example of the occurrence of a multi-step delocalisation process in actinide metals which normally have localised 5f electrons.

Overall, such high-pressure studies, which reach out to new pressure limits, require synchrotron radiation to obtain the quality data that are needed. Synchrotron radiation offers a new potential for establishing important structural and electronic behaviour of actinides. Such studies are important not only for advancing actinide science, but also for providing new information for evaluating theoretical concepts/calculations. Hopefully, these studies will promote the convergence of experimental findings and theoretical views regarding the behaviour of 5f electrons under pressure.

Acknowledgements

This work is supported by the Division of Chemical Sciences, Geosciences and Biosciences, Office of Basic Energy Sciences, US Department of Energy, under contract DE-ACO5-00OR22725 with Oak Ridge National Laboratory, managed/operated by UT-Battelle, LLC, and also sponsored by the European Commission. The beam time allocated at the ID30 beam line at the ESRF for performing the americium experiments is also acknowledged, as is the Health Physics coverage and co-operation provided by P. Berkvens and P. Colomp at the ESRF.

REFERENCES

[1] R.G. Haire, in *Actinides in Perspective*, N.M. Edelstein, ed., Pergamon Press (New York, 1982), pp. 309-342.

[2] R.G. Haire, *J. Less-common Metals*, 121, 379-398 (1986).

[3] J.C. Spirlet and O. Vogt, in *Handbook on the Physics and Chemistry of the Actinides*, A.J. Freeman and G.H. Lander, eds., North-Holland (Amsterdam, 1984), p. 79 and references therein.

[4] Design of Prof. Ruoff, Cornell University, NY.

[5] Design of K. Syassen and W.B. Holzapfel.

[6] Mao-Bell Megabar Cell, Geophysical Laboratory, Washington D.C.

[7] M. Thoms, S. Bauchau, D. Häusermann, M. Kunz, T. Le Bihan, M. Mezouar, D. Strawbridge, *Nuclear Instruments and Methods in Physics Research*, A 413, 175 (1998).

[8] U. Benedict and W.B. Holzapfel, in *Handbook on the Physics and Chemistry of Rare Earths*, K. Gschneider, Jr., L. Eyring, G.H. Lander, G.R. Choppin, eds., Elsevier Science (Netherlands, 1993), Vol. 17, Chap. 113, pp. 245-300 and references therein.

[9] R.G. Haire, in *Resources, Science Technology and Applications*, R. Bautista, N. Jackson, eds., TMS (Pennsylvania, 1991), pp. 449-462 and references therein.

[10] U. Benedict, in *Handbook on the Physics and Chemistry of the Actinides*, A.J. Freeman and G.H. Lander, eds., Elsevier Science (Netherlands, 1987), Chapter 3, pp. 227-269 and references therein.

[11] K.A. Gschneider, Jr. and F.W. Calderwood, in *Handbook on the Physics and Chemistry of the Rare Earths*, K.A. Gschneider, Jr. and L. Eyring, eds., North-Holland (Amsterdam, 1986), Vol. 8, Chapter 54, pp. 156-160 and references therein.

[12] M.I. McMahon and R.J. Nelmes, *Phys. Rev. Lett*., 78, 3883 (1997).

[13] S. Heathman, R.G. Haire, T. Le Bihan, A. Lindbaum, K. Litfin, Y. Méresse and H. Libotte, *Phys. Rev. Lett*., 85, No. 14, 2961-2964 (2000).

[14] J. Akella, Q. Johnson, W. Thayer and R.N. Schock, *J. Less-common Metals*, 68, 95 (1979).

[15] J. Akella, Q. Johnson and R.N. Schock, *J. Geophys. Res.*, B85, 7056 (1980).

[16] R.L. Reichlin, J. Akella, D. Smith and M. Schwab, LBL-12441, pp. 218-219 (1981).

[17] R.B. Roof, R.G. Haire, D. Schiferel, L.A. Schwalbe, E.M. Kmeto and J.L. Smith, *Science*, 207, 1353 (1980).

[18] R.B. Roof, *J. Applied Cryst*., 14, 447 (1981).

[19] R.B. Roof, *Z. Zristallographie*, B15, 307 (1982).

[20] U. Benedict, J.P. Itíe, C. Dufour, S. Dabos and J.C. Spirlet, in *Americium and Curium Chemistry and Technology*, N.M. Edelstein, J.D. Navratil and W.W. Schultz, eds., Reidel, Dordrecht (Boston, 1985), pp. 221-224.

[21] U. Benedict, J.P. Itíe, C. Dufour, S. Dabos and J.C. Spirlet, *Physica B*, 139/140, 284 (1986).

THIN FILMS OF ACTINIDES: MODEL SYSTEMS IN FUNDAMENTAL AND APPLIED RESEARCH

T. Gouder,[1] L. Havela,[1,2] F. Wastin[1] and J. Rebizant[1]
[1]European Commission, Joint Research Centre, Institute for Transuranium Elements
Post Box 2340, D-76175 Karlsruhe, Germany
[2]Department of Electronic Structures, Charles University
Ke Karlovu 5, CZ-121 16 Prague 2, Czech Republic

Abstract

The surface of actinide solids plays an important role in determining their chemical behaviour. In particular the long-term stability of waste materials strongly depends on aspects of the microstructure of surface layers such as defects, grain boundaries and local heterogeneities. We use thin films for studying these aspects both in simple model systems and in more complex real-world systems. We are interested in particular in variable electronic structure in surface layers, surface reconstruction, over-layer/substrate bonding and the electrochemical and leaching properties of the surface layers. The films are produced *in situ* by sputter deposition from small actinide targets (100 mg to 2 g), and studied by photoelectron spectroscopy (XPS and UPS), Auger electron spectroscopy (AES) and ion scattering spectroscopy (ISS). Two examples describing our approach are given below.

Thin films of Pu have been deposited on various substrates: Mg, Al and single crystalline Si(111). For low thickness (around one mono-layer) the films lose their bulk electronic structure. The 5f electrons which in the bulk are de-localised tend to localisation, i.e. they no longer participate in the chemical bonding. This phenomenon is more pronounced for Al and Si substrates, where the surface films seem to spread out because of good over-layer/substrate bonding, while for Mg thick, bulk-like clusters seem to be formed. For thicker films the 5f electrons generally become itinerant but show unexpected temperature dependence, which is attributed to the highly correlated nature of the 5f states, i.e. the closeness to the localisation threshold. Experiments are planned to probe the chemical reactivity of these films.

We investigated the evolution of the electronic structure and chemical reactivity in various U-Ga compounds: UGa_2, UGa_3 inter-metallics, and thin films of U on Ga. It was shown that the surface reactivity of the inter-metallics depends strongly on the deposition temperature. At high temperatures (573 K) a mono-layer of Ga forms at the top surface, as shown by ISS. This leads to a strong passivation of the systems. We were faced with an unusual situation in which working at high temperatures resulted in cleaner films than working at room temperature. The surface reactivity was further probed by adsorption experiments of CO.